Robust Higher-Order Spatial Iterative Learning Control for Additive Manufacturing Systems

Zahra Afkhami, *Member, IEEE*, David J. Hoelzle, *Member, IEEE*, and Kira Barton, *Senior Member, IEEE*

Abstract— In this article, a higher-order spatial iterative learning control (HO-SILC) scheme is proposed, targeting heightmap tracking for a class of 3-D structures fabricated by repetitive addition of material in a layer-by-layer fashion using additive manufacturing (AM) technology. AM processes are innately iteration-varying, resulting in large model uncertainties due to iteration-varying system parameters and surface variations. HO-SILC has been shown to be useful in repetitive systems with model uncertainties by improving system performance with respect to convergence speed and robustness. In this article, HO-SILC is used to iteratively construct a feedforward control signal to improve part quality in multilayered AM constructs. The system dynamics are approximated by discrete 2-D spatial convolution kernels that incorporate in-layer and layer-to-layer variations. The proposed HO-SILC framework incorporates data available from previously printed devices, as well as multiple previously printed layers, to enhance the overall performance. The condition for robust monotonic convergence (RMC) of the iteration-varying HO-SILC algorithm is based on the Lyapunov stability criteria. Simulation results of an AM process termed electrohydrodynamic jet (e-jet) printing demonstrate that a well-designed HO-SILC framework is effective and can improve the performance by 60%. In addition, HO-SILC is robust to iteration-varying model uncertainties, especially at higher layers where iteration-varying surface variations are more pronounced.

Index Terms— Intelligent and flexible manufacturing, learning control, Lyapunov methods, stability of linear systems.

I. INTRODUCTION

IN THE past few decades, there has been a growing interest in additive manufacturing (AM) technologies due to their potential for simplified processing and design space freedom. Through AM, a printed device, which could be structural or contain other functional characteristics, such as a sensor, is generated by selective addition of material on the surface in a layer-by-layer fashion [1], [2], [3]. Due to the wide range of materials that can be used in AM processes, AM-fabricated devices, specifically those from jet-based printing processes, have been used in diverse applications, including flexible electronics [4], biological sensors [5], and optical filters [3]. The performance of such devices depends on the uniformity and consistency of the printed layers [2]. However, for most AM systems, it is very difficult to actuate and sense in real time [6]. The output and subsequent error measurements are only available after the material is deposited onto the substrate. In addition, most AM processes are iteration-varying, with the system parameters and plant dynamics changing from device to device and layer to layer. Thus, the behavior of the printing at a given layer depends on material and topography interactions from previous layers, which vary in real-world applications. Control methods that leverage the iterative nature of these processes in the presence of disturbances are needed.

Iterative learning control (ILC) is a run-to-run control technique that has been widely used in systems with repetitive characteristics in order to achieve accurate output tracking of a reference trajectory over a short number of iterations [7]. Temporal ILC uses past information in the time domain in order to build an appropriate feedforward control signal with the aim of ensuring convergence of the tracking error from iteration to iteration. Previous studies [8], [9], [10] have considered ILC architectures that address bounded iteration-varying model parameters, and provide convergence guarantees to a bounded neighborhood of a nominal system.

First-order ILC (FO-ILC) leverages the data from the most recent iteration, to construct an optimal feedforward signal. While FO-ILC has proven to be useful for reference tracking of repetitive systems, it might lose performance when uncertainties are high. To achieve better performance with respect to convergence speed, higher-order ILC (HO-ILC) has been developed, where the feedforward signal is synthesized using historical data from multiple iterations [10], [11], [12], [13], [14], [15]. There have been several attributes stated in the literature that motivate the implementation of HO-ILC over FO-ILC. Phan and Longman [15] presented anecdotal evidence of merit to justify either HO- or FO-ILC depending on the situation. However, Bien and Huh [13] and Chen et al. [14] argued that an HO-ILC framework demonstrated better convergence speed and robustness than an FO-ILC framework, while Moore [16] asserted that the real motivation behind the use of HO-ILC was to reduce the effects of disturbances and noise. Similarly, Bu et al. [11], Wei and Li [12], and Norrlof and Gunnarsson [17] claimed that an HO-ILC design achieved faster convergence as compared with an FO-ILC framework due to the effects of learning over several previous iterations. Importantly, these methods have

primarily been considered for performance improvements in the temporal domain.

There has been some work in the literature focused on extending temporal ILC to the spatial domain, such that system parameters can be defined based on 2-D spatial coordinates, x and y [18]. In these processes, the ILC algorithms aim to decrease the 2-D spatial tracking errors $e(x, y)$ from iteration to iteration. Spatial ILC (SILC) has been demonstrated for topography control in AM processes [18]; however, current SILC frameworks have been designed for single-layer material deposition [18], [19], [20]. In many AM structures, the devices are fabricated by repetitive material deposition over existing layers. The printing of multiple layers leads to surface variations due to previous layer topography and results in iteration-varying dynamics and model uncertainties. In recent years, the SILC framework has been extended to consider model uncertainties due to iteration-varying system parameters for single-layer structures [19]. The iteration-varying SILC algorithm in [19] enables robust monotonic convergence (RMC) for a run-to-run AM process based on Lyapunov stability criteria.

Our previous work introduced a first-order SILC (FO-SILC) framework [21] that considered in-layer and layer-to-layer dynamics to achieve uniformly printed layers in multimaterial 3-D structures. The control input of the proposed FO-SILC was updated from the previously printed device information along the device axis (j horizontal) within the same layer l. A drawback of this previous framework stems from the additive process itself. The FO-SILC framework only leveraged the errors from the previous layer to derive current layer errors, $\Delta e_{l,j}(x, y)$. This approached ignored the buildup of errors that can occur from layer to layer, potentially causing large deviations from the desired total height. Importantly, the learning process can be more complicated at higher layers in which large surface variations have resulted from the accumulation of errors, leading to large model uncertainties. A controller should be able to compensate for the total accumulated error $e_{l,j}(x, y)$ in the layer direction l (vertical z-axis), which is especially important in cases when a large number of layers are deposited. Thus, new theories are needed to control in-layer errors as well as the total accumulated error in multilayered structures. In this article, we propose the use of higher-order SILC (HO-SILC) to achieve better convergence performance as compared with FO-SILC [11] due to the additional information that is leveraged from previous layers.

This article extends our earlier work in [21] and [22] toward the development of a multidimensional, HO-SILC framework in the lifted and frequency domains. The proposed HO-SILC scheme encompasses interval model uncertainties and spatially varying dynamics arising in the printing of multilayered components due to droplet-to-droplet coalescence effects or unevenness of the previous layers. Here, we investigate different linear/nonlinear models to describe material spreading in multilayered structures, and evaluate the performance of the proposed HO-SILC when these different models are used. Our proposed approach differs from those in the literature [17], [23], since the transfer operator matrices

that convert the HO-SILC to an FO-SILC for stability analysis are constructed based on the layer-by-layer nature of the AM process. The proposed HO-SILC framework incorporates *vertical learning* through the combined effect of previous layer spatial dynamics and layer-to-layer learning (learning from previous layers in the same device) and *horizontal learning* from device to device (in the same layer). The proposed HO-SILC differs from traditional HO-ILC frameworks due to the 2-D aspect of the learning. Traditional HO-ILC considers information from previous data across the iteration axis. HO-SILC incorporates learning over two axes, along the device axis (j horizontal) and over multiple iterations in the layer axis (l vertical), which has similarities to the 2-D adaptive ILC framework in [24]. In addition, design ideas are presented to explore the effect of HO-SILC parameters on robustness and speed of convergence. The contributions of this work include the following:

1) development of an HO-SILC framework for controlled printing of 3-D structures that combines device-to-device and layer-to-layer learning in the lifted and frequency domains, while considering iteration-varying spatial dynamics;
2) a detailed methodology for transforming HO-SILC of AM processes to an FO-SILC representation for stability and robustness analysis;
3) development of a design methodology for deriving learning filters that directly embed stability criteria for nominal HO-SILC systems;
4) design of a boundary prediction of the maximum allowable uncertainty around a nominal plant for monotonic convergent of the iterative norm-optimal HO-SILC algorithm.

Simulation results using a model of an electrohydrodynamic jet (e-jet) printing process are used to demonstrate the feasibility of the proposed HO-SILC framework for AM process control. In the absence of experimental data, the simulation environment approximates the *true* model using a nonlinear model based on the design presented in [25], which incorporates nonlinear dynamics, such as surface effects of the liquid droplets and the effect of previous layer surface variations. Note that for simplicity and fast computation purposes, a nominal model is used to design the controller.

II. PRELIMINARIES

In this section, preliminary notations and definitions that will be used in the rest of the paper will be defined.

A. Notation

The finite set of $\mathbb{Z}_n$ for an odd and positive integer n is defined as follows:

$$\mathbb{Z}_n \triangleq \left\{ \frac{1-n}{2}, \frac{3-n}{2}, \ldots, \frac{n-3}{2}, \frac{n-1}{2} \right\}$$

with $\mathbb{Z}_1 \triangleq \{0\}$. A generic scalar function $p(x, y)$ sampled at discrete values can be combined in the matrix form, as shown in the equation at the bottom of the next page, where finite support of p is $\text{supp}(p) = \{(x, y) \in \mathbb{Z}_{n_x} \times \mathbb{Z}_{n_y} : p(x, y) \neq 0\}$.

Setting n_x and n_y as positive odd integers makes the central location of p at $(0, 0)$. An example of this generic function is the heightmap in μ-AM systems defined as a 2-D array of printed droplets in the spatial domain. The 2-D discrete Fourier transform (DFT) representation of $p(x, y)$ is defined as follows:

$$P(u, v) = \sum_{x=0}^{n_x-1} \sum_{y=0}^{n_y-1} \left(p\left(x + x^\Delta, y + y^\Delta\right) e^{-i2\pi \left(\frac{ux}{n_x} + \frac{vy}{n_y}\right)} \right)$$

where $x^\Delta = \lfloor (n_x/2) \rfloor + 1$, $y^\Delta = \lfloor (n_y/2) \rfloor + 1$, and $\lfloor \cdot \rfloor$ is the floor operator. Hereafter, we will use capital italic font to show the frequency domain variables.

A vectorization operator $\nu(\cdot)$ can be applied to a matrix, $P \in \mathbb{R}^{n_x \times n_y}$, to convert the matrix into a column vector form, $\mathbf{P} \in \mathbb{R}^{n \times 1}$, given as follows:

$$\mathbf{P} \triangleq \nu(P) = \text{vec}(P^\mathsf{T})$$

where $\text{vec}(\cdot)$ is the conventional columnwise vectorization operator. The Frobenius norm of a matrix $P \in \mathbb{R}^{n_x \times n_y}$ is equal to the l_2 norm of the vectorized matrix, $\|P\|_F = \|\mathbf{P}\|_2$.

B. Definitions

1) $\text{circ}(p_1, p_2, \ldots, p_n)$ is defined as a block circulant matrix with square submatrices of the same size, $p_1, p_2, \ldots, p_n$, where n is an odd number. The ith block of the middle column in $\text{circ}(p_1, p_2, \ldots, p_n)$ is always p_i [19]. For example, if $n = 3$

$$\text{circ}(p_1, p_2, p_3) = \begin{bmatrix} p_2 & p_1 & p_3 \\ p_3 & p_2 & p_1 \\ p_1 & p_3 & p_2 \end{bmatrix}.$$

2) A matrix is said to be block circulant with circulant blocks (BCCBs) if it is defined as follows:

$$H \triangleq \text{circ}\left(H_{\frac{1-n_x}{2}}, H_{\frac{3-n_x}{2}}, \ldots, H_{\frac{n_x-1}{2}}\right) \in \mathbb{R}^{n \times n}$$

$$H_i \triangleq \text{circ}\left(h\left(i, \frac{1-n_y}{2}\right), h\left(i, \frac{3-n_y}{2}\right),\right.$$
$$\left. \ldots, h\left(i, \frac{n_y-1}{2}\right)\right), \quad \in \mathbb{R}^{n_y \times n_y}$$

where $h(x, y)$ is a discrete function, with the same support as p. Note that the l_2 norm of H equals the maximum modulus of its DFT representation; i.e., $\|H\|_2 = \|H(u, v)\|_\infty = \max_{(u,v)} |H(u, v)|$. The BCCB property of a matrix makes fast Fourier transforms (FFTs) possible, which has been demonstrated to be computationally less expensive in calculating matrix products and norms [18], especially in applications with large n values.
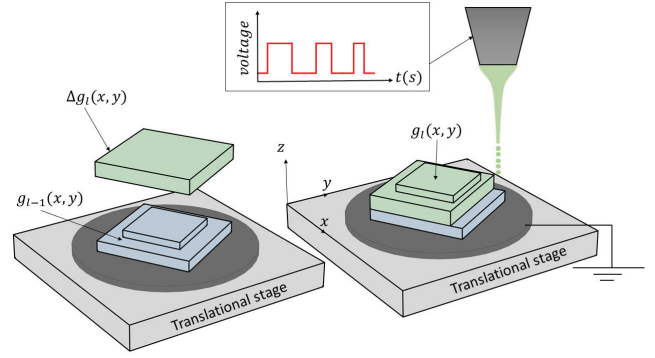

Fig. 1. Schematic of AM spatial dynamics described in (1).

III. GENERAL ITERATION-VARYING AM SYSTEM

In order to enable automated topography control for droplet-based AM processes, models that describe heightmap evolution in a layer-by-layer fashion are needed. Examples of these models are presented in [25], [26], [27], [28], and [29]. In these models, the printed topography of the next layer, $g_{l+1} \in \mathbb{R}^{n_x \times n_y}$, is a linear or nonlinear function of the current layer topography, $g_l \in \mathbb{R}^{n_x \times n_y}$, and the input signal of the next layer, $f_{l+1} \in \mathbb{R}^{n_x \times n_y}$. l is the layer number. The following assumptions are considered for the AM process described in Fig. 1.

1) A_1: The spreading behavior of a printed material on a flat surface is different from that on a nonflat surface [29].

2) A_2: The plant spatial dynamics are causal in the temporal and noncausal in the spatial domain, meaning that the applied input at a given position will affect the output in the advanced layers and surrounding coordinates [29].

3) A_3: The plant matrix (H) is considered bounded input, bounded output (BIBO) stable, meaning that there exist positive finite scalars ξ and ζ, such that given a bounded input, $\|\mathbf{f}_l(x, y)\| < \xi$, the resulted output will always be bounded, $\|\mathbf{g}_l(x, y)\| < \zeta$, $\forall (x, y) \in \mathbb{R}^{n_x \times n_y}$ (ξ and ζ are independent of l).

Assumptions $\mathbf{A}_1$ and $\mathbf{A}_2$ denote that the spatial dynamics of a given plant (H) are a function of previous layer topography ($\mathbf{g}_{l-1}$) and the surrounding environment. Assumption $\mathbf{A}_3$ holds for the additive system described in Fig. 1, given that material addition to the substrate is bounded by a predefined volume of available material. Furthermore, because of actuator constraints, the input is limited by an upper bound [19]. A simple linear representation of such a model is described as follows:

$$\mathbf{g}_l = \mathbf{g}_{l-1} + H(\mathbf{g}_{l-1})\mathbf{f}_l \tag{1}$$

$$p(x, y) = \begin{bmatrix} p\left(\frac{1-n_x}{2}, \frac{1-n_y}{2}\right) & p\left(\frac{1-n_x}{2}, \frac{3-n_y}{2}\right) & \cdots & p\left(\frac{1-n_x}{2}, \frac{n_y-1}{2}\right) \\ p\left(\frac{3-n_x}{2}, \frac{3-n_y}{2}\right) & p\left(\frac{3-n_x}{2}, \frac{3-n_y}{2}\right) & \cdots & p\left(\frac{3-n_x}{2}, \frac{n_y-1}{2}\right) \\ \vdots & \vdots & \ddots & \vdots \\ p\left(\frac{n_x-1}{2}, \frac{1-n_y}{2}\right) & p\left(\frac{n_x-1}{2}, \frac{3-n_y}{2}\right) & \cdots & p\left(\frac{n_x-1}{2}, \frac{n_y-1}{2}\right) \end{bmatrix}$$

where $\mathbf{f}_l \triangleq v(f_l(x, y)) \in \mathbb{R}^{n \times 1}$ is the input signal, $\mathbf{g}_l \triangleq v(g_l(x, y)) \in \mathbb{R}^{n \times 1}$ is the output, and $H \in \mathbb{R}^{n \times n}$ is the interval plant matrix that describes the relation between system input and output. We will use H_{l-1} instead of $H(\mathbf{g}_{l-1})$ for brevity. H is an interval matrix if all of its elements are interval parameters. In other word, the interval H is a member of the following matrix set:

$$H^I = \left\{ H \in \mathbb{R}^{n \times n} \mid \underline{H} \preceq H \preceq \overline{H} \right\}$$

where $\preceq$ is elementwise inequality. Note that the plant bounds are known and fixed properties of the iteration-varying system that can be measured by running the additive process described in (1) multiple times and measuring maximum and minimum droplet spreading on spatially varying surfaces [29]. For a general AM process, we are interested in controlling the heightmap increment ($\Delta \mathbf{g}_l \triangleq \mathbf{g}_l - \mathbf{g}_{l-1}$) with respect to the previous layer described as follows:

$$\Delta \mathbf{g}_l = H_{l-1} \mathbf{f}_l, \quad H_{l-1} \in H^I \tag{2}$$

where H^I is the interval set associated with H_{l-1}. In Section VI-A, we will describe in detail the different available models for the additive process in (1).

IV. HO-SILC DESIGN FOR MULTILAYER STRUCTURES

In our prior work in [21], we derived an FO-SILC framework that used the information from a previous iteration in the device axis (horizontal learning) to construct the feedforward input signal. In this work, we extend that framework by adding layer-to-layer learning (vertical direction), as presented in Fig. 2(b) and (c). Note that both SILC frameworks incorporate the effect of previous layer contours through construction of the plant model in (1). We term the proposed SILC algorithm HO-SILC, because learning occurs over one iteration in the device axis (j, horizontal) and $l-1$ iterations in the layer axis (l, vertical). For a multilayered structure, as shown in Fig. 2(a), the following HO-SILC update law is proposed:

$$\mathbf{f}_{l,j+1} = \left(L_f^h \mathbf{f}_{l,j} + L_e^h \Delta \mathbf{e}_{l,j} \right)$$
$$+ \sum_{i=1}^{l-1} \left(L_f^{v_i} \mathbf{f}_{l-i,j+1} + L_e^{v_i} \Delta \mathbf{e}_{l-i,j+1} \right) \tag{3}$$

with L_f^h, L_e^h, $L_f^{v_i}$, and $L_e^{v_i} \in \mathbb{R}^{n \times n}$ defined as the horizontal input and error filters, and vertical input and error filters. Note that in (3), printing is in the horizontal direction from device to device. The update law in (3) is suitable for devices, such as [21] and [30], in which multiple materials are printed at specific layers, or the reference incremental height is changing from layer to layer.

A. Design of Learning Filters

There are many different methods that can be employed from temporal ILC to design the input and error filters in (3), such as proportional-type ILC, model inversion, and Q-filter design [31]. Here, we implement a norm optimal-SILC (NO-SILC) algorithm [18], which seeks to minimize a quadratic

cost function in the spatial domain. We define a weighted error vector $\mathbf{e}_{l,j+1}^w$, as follows:

$$\mathbf{e}_{l,j+1}^w \triangleq \Delta \mathbf{e}_{l,j+1} + \alpha_1 \Delta \mathbf{e}_{l-1,j+1} + \cdots + \alpha_{l-1} \Delta \mathbf{e}_{1,j+1}$$
$$\vec{\alpha} \triangleq [\alpha_0, \alpha_1, \alpha_2, \ldots, \alpha_{l-1}]^T \tag{4}$$

where the values of $\alpha_i \in [0, 1]$ are layer-varying user-defined control parameters. The quadratic cost function that is minimized to solve for the NO-SILC learning filters is defined as follows:

$$\mathcal{J} = q \mathbf{e}_{l,j+1}^{w^T} \mathbf{e}_{l,j+1}^w + r \left(\mathbf{f}_{l,j+1} - \mathbf{f}_{l,j} \right)^T \left(\mathbf{f}_{l,j+1} - \mathbf{f}_{l,j} \right)$$
$$+ s \mathbf{f}_{l,j+1}^T \mathbf{f}_{l,j+1} + \sum_{i=1}^{l-1} \beta_i r \left(\mathbf{f}_{l,j+1} - \mathbf{f}_{l-i,j+1} \right)^T$$
$$\times \left(\mathbf{f}_{l,j+1} - \mathbf{f}_{l-i,j+1} \right) \tag{5}$$

where q, s, and r are real positive scalars that penalize the weighted error, input signal, and change in the input signal from iteration to iteration. The values of $\beta_i \in [0, 1]$ are layer-varying user-defined parameters to weight the influence of previous layer input signals, such that $\vec{\beta} \triangleq [\beta_1, \beta_2, \ldots, \beta_{l-1}]^T$. In order to emphasize more recent layers, we set $\alpha_i' = (\alpha^i / \|\vec{\alpha}\|)$ and $\beta_i' = (\beta^i / \|\vec{\beta}\|)$, with $\alpha, \beta \in [0, 1]$. Note that if $\alpha = 1$ in (4), the cost function (5) is optimized over the total error.

1) Lifted-Domain Learning Filters: Given that $\Delta \mathbf{g}_l^d$ is the desired output at layer l, the predicted incremental error can be expressed as follows:

$$\Delta \mathbf{e}_{l,j} = \Delta \mathbf{g}_l^d - H_{l-1,j} \mathbf{f}_{l,j}. \tag{6}$$

Using the assumption of iteration-invariant desired reference trajectories, we can relate two successive errors (iteration to iteration) within the same layer using the following equation:

$$\Delta \mathbf{e}_{l,j+1} = \Delta \mathbf{e}_{l,j} + H_{l-1,j} \mathbf{f}_{l,j} - H_{l-1,j+1} \mathbf{f}_{l,j+1}. \tag{7}$$

Substituting (4) and (7) into (5) and setting the partial derivatives of $\mathcal{J}$ with respect to $\mathbf{f}_{l,j+1}$ equal to zero, the following relationships can be obtained for the filters based on the nominal plant, H_0:

$$L_f^h = \left(\left(s + r + r \sum_{i=1}^{l-1} \beta_i' \right) I + \alpha_0' q H_0^T H_0 \right)^{-1}$$
$$\times \left(r I + \alpha_0' q H_0^T H_0 \right) \tag{8a}$$

$$L_e^h = \left(\left(s + r + r \sum_{i=1}^{l-1} \beta_i' \right) I + \alpha_0' q H_0^T H_0 \right)^{-1} \alpha_0' q H_0^T \tag{8b}$$

$$L_f^{v_i} = \left(\left(s + r + r \sum_{i=1}^{l-1} \beta_i' \right) I + \alpha_0' q H_0^T H_0 \right)^{-1} \beta_i' r I \tag{8c}$$

$$L_e^{v_i} = \frac{\alpha_i'}{\alpha_0'} L_f^h. \tag{8d}$$

2) Frequency-Domain Learning Filters: If the plant matrix in (1) is BCCB, the learning filters and the update law in (3) and (8) have frequency representations, which enable us to use computationally efficient FFT methods. The frequency domain
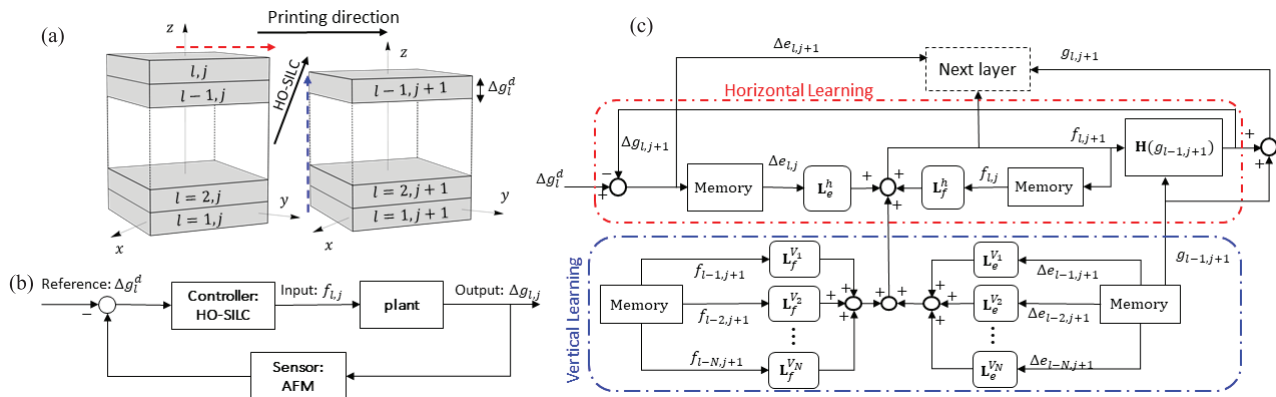
Fig. 2. Closed-loop control of AM process. (a) Learning happens from layer to layer (vertical) and device to device (horizontal) to control material deposition in 3-D structures. (b) HO-SILC is used as a recursive control strategy to close the loop. (c) Standard HO-SILC block diagram. l denotes the layer index, and j denotes the iteration index.

representation of the learning filters in (8) for a BCCB plant matrix is presented as follows:

$$
L_f^h (u, v) = \frac{\alpha_0' q H_0^* \circ H_0 + r 1_{n \times n}}{\alpha_0' q H_0^* \circ H_0 + \left(s + r + r \sum_{i=1}^{l-1} \beta_i'\right) 1_{n \times n}} (u, v)
$$

(9a)

$$
L_e^h (u, v) = \frac{\alpha_0' q H_0^*}{\alpha_0' q H_0^* \circ H_0 + \left(s + r + r \sum_{i=1}^{l-1} \beta_i'\right) 1_{n \times n}} (u, v)
$$

(9b)

$$
L_f^{v_i} (u, v) = \frac{r \beta_i' 1_{n \times n}}{\alpha_0' q H_0^* \circ H_0 + \left(s + r + r \sum_{i=1}^{l-1} \beta_i'\right) 1_{n \times n}} (u, v)
$$

(9c)

$$
L_e^{v_i} (u, v) = \frac{\alpha_i'}{\alpha_0'} L_e^h (u, v), \quad i = 1, \dots, l-1
$$

(9d)

where $\circ$ is the Hadamard or entrywise product of two matrices, and H_0 is the frequency domain representation of the nominal plant. A full description of the frequency domain conversion can be found in [18]. $L_f^h, L_e^h, L_f^{v_i},$ and $L_e^{v_i} \in \mathbb{R}^{n_x \times n_y}$ are 2-D DFTs of the learning filters in (8). Because of the BCCB structure of H_0 and the learning filters, the update law in (3) for the BCCB plant model can be equivalently represented in the frequency domain as follows:

$$
\begin{aligned}
&F_{l, j+1} (u, v) \\
&= \left(L_f^h \circ F_{l, j} + L_e^h \circ \Delta E_{l, j} \right) (u, v) \\
&\quad + \sum_{i=1}^{l-1} \left(L_f^{v_i} \circ \Delta F_{l-i, j+1} + L_e^{v_i} \circ \Delta E_{l-i, j+1} \right) (u, v).
\end{aligned}
$$

(10)

B. HO-SILC Transformation to FO-SILC

HO-ILC algorithms generally have faster convergence as compared with FO-ILC, because HO-ILC uses the information from multiple previous trials to construct the control signal. In the literature, there are very few examples of MC of HO-ILC systems [10], [17], while the stability condition of FO-ILC is well described. It is possible to leverage the proofs for FO-ILC to analyze stability of an HO-ILC system by converting the HO-ILC algorithm to an FO-ILC framework.

In this section, we follow methods developed in [8], [23], and [32] to convert the HO-SILC framework in (3) to an FO-SILC. This modified FO-ILC framework will then be used to investigate stability margins for the iteration-varying model described in (2). The approach taken here is a bit different than [8], [23], and [32]. The transfer functions from HO-SILC to FO-SILC are constructed based on the layer-by-layer nature of AM process, such that the FO-SILC system incorporates learning along the iteration axis, j, as well as the layer axis, l.

The HO-SILC algorithm defined in (3) can be expressed based on the closed-loop plant matrices, by inserting (6) into (3) as follows:

$$
\begin{aligned}
\mathbf{f}_{l, j+1} &= T_{l-1, j}^h \mathbf{f}_{l, j} + \sum_{i=1}^{l-1} T_{l-i-1, j+1}^{v_i} \mathbf{f}_{l-i, j+1} \\
&\quad + \left(L_e^h + \sum_{i=1}^{l-1} L_e^{v_i} \right) \Delta \mathbf{g}^d
\end{aligned}
$$

(11)

with $T_{l, j}^h = L_f^h - L_e^h H_{l, j}$ and $T_{l-i-1, j}^{v_i} = L_f^{v_i} - L_e^{v_i} H_{l-i-1, j}$ being the closed-loop horizontal and vertical plant matrices, respectively. Equation (11) can be further simplified by concatenating the input signals over the vertical axis, l, such that

$$
\begin{aligned}
\mathbf{z}_{l, j+1} &= D_{l, j} \mathbf{z}_{l, j} + K_{l, j} \mathbf{z}_{l, j+1} + \mathbf{C}_l \\
\mathbf{z}_{l, j} &= \left[\mathbf{f}_{l, j}^T, \dots, \mathbf{f}_{2, j}^T, \mathbf{f}_{1, j}^T \right]^T \in \mathbb{R}^{\ln \times 1} \\
\mathbf{z}_{l, \infty} &= (I - D_{l, \infty} - K_{l, \infty})^{-1} \mathbf{C}_l
\end{aligned}
$$

(12)

where $D_{l, j} \in \mathbb{R}^{\ln \times \ln}$, $K_{l, j} \in \mathbb{R}^{\ln \times \ln}$, and $\mathbf{C}_l \in \mathbb{R}^{\ln \times 1}$ are a diagonal block matrix, upper triangular block matrix, and constant vector, respectively

$$
D_{l, j} = \begin{bmatrix} T_{l-1, j}^h & 0 & \cdots & 0 \\ 0 & \ddots & & \vdots \\ \vdots & & T_{1, j}^h & 0 \\ 0 & \cdots & & T_{0, j}^h \end{bmatrix}
$$

(13a)

This article has been accepted for inclusion in a future issue of this journal. Content is final as presented, with the exception of pagination.

6

IEEE TRANSACTIONS ON CONTROL SYSTEMS TECHNOLOGY

$$K_{l,j} = \begin{bmatrix} 0 & T_{l-2,j+1}^{v_1} & T_{l-3,j+1}^{v_2} & \cdots & T_{1,j+1}^{v_{l-2}} & T_{0,j+1}^{v_{l-1}} \\ & 0 & T_{l-3,j+1}^{v_1} & \cdots & T_{1,j+1}^{v_{l-2}} & T_{0,j+1}^{v_{l-2}} \\ & & \ddots & \ddots & \vdots & \vdots \\ \vdots & & & 0 & T_{1,j+1}^{v_1} & T_{0,j+1}^{v_2} \\ & & & & 0 & T_{0,j+1}^{v_1} \\ 0 & & \cdots & & & 0 \end{bmatrix}$$

$$(13b)$$

$$\mathbf{C}_l = \begin{bmatrix} \left(L_e^h + L_e^{v_1} + \cdots + L_e^{v_{l-1}} \right) \Delta \mathbf{g}^d \\ \vdots \\ \left(L_e^h + L_e^{v_1} + L_e^{v_2} \right) \Delta \mathbf{g}^d \\ \left(L_e^h + L_e^{v_1} \right) \Delta \mathbf{g}^d \\ L_e^h \Delta \mathbf{g}^d \end{bmatrix}. \qquad (13c)$$

Equation (12) can be further simplified to the following FO-SILC format:

$$\mathbf{z}_{l,j+1} = F_{l,j} \mathbf{z}_{l,j} + \mathbf{F}_r$$
$$F_{l,j} = \left(I - K_{l,j} \right)^{-1} D_{l,j}$$
$$\mathbf{F}_r = \left(I - K_{l,j} \right)^{-1} \mathbf{C}_l. \qquad (14)$$

We used the same notation as [8] and [17] for transfer matrices $\mathbf{F}_{l,j}$ and $\mathbf{F}_r$. The FO-SILC algorithm in (14) will be used in the following section to investigate the asymptotic and monotonic properties of the HO-SILC update law in (11) following methods described in [8], [10], [17], and [19].

V. Stability and Convergence

In most control systems, a fundamental goal is to guarantee the convergence of the tracking error to zero or within a neighborhood of a nominal value over a small number of iterations. Asymptotic stability of iteration-varying systems requires the joint spectral radius of the iterative plant to be less than one, which is a difficult problem [19], [33]. In many manufacturing applications, such as the optical sensor presented in [2], large transient errors may introduce failures in the functional capabilities of the printed device. Therefore, the controller should be designed to regulate material deposition, such that the layer errors decrease from iteration to iteration and layer to layer. In this work, we focus on monotonic stability of iterative systems subjected to bounded model uncertainties, which is an often desirable property for AM processes. We combine the methods developed in [10], [17], and [19] to derive stability conditions for HO-SILC processes subjected to iteration-varying model uncertainties. First, we design the learning filters, such that the nominal system is stable. Then, a stability radius, r_{AIU}, is designed based on the Lyapunov equation, such that the iterative system remains stable as long as the magnitude of model uncertainties is less than the stability radius at all iterations. We follow the method developed by Norrlof and Gunnarsson [17] to convert HO-SILC to an FO-SILC. Then, we follow [10] and [19] to design the stability margins of the converted FO-SILC subjected to interval uncertainty.

Theorem 1: The system in (1) controlled by the FO-SILC in (14) [or HO-SILC in (11)] is monotonically convergent in

the l_p norm, $\|\mathbf{Z}_{l,j+1} - \mathbf{Z}_{l,\infty}\|_p < \|\mathbf{Z}_{l,j} - \mathbf{Z}_{l,\infty}\|_p$, if

$$\|F_{l,j}\|_p < 1 \quad \forall l, j$$
$$\|F_r\|_p < \xi \qquad (15)$$

where ξ is positive scalar that ensures $\|F_r\|_p$ remains bounded.

Corollary 1: The monotonic stability condition in (15) can be expressed as follows:

$$\text{RMC} \triangleq \frac{1 - \|K_{l,j}\|_p^{l-1}}{1 - \|K_{l,j}\|_p} \times \|D_{l,j}\|_p < 1 \quad \forall l, j. \qquad (16)$$

Proof: $K_{l,j}$ is a strictly upper triangular block matrix containing block matrices of higher-order terms, $T_{l,j}^{v_i} \in \mathbb{R}^{n \times n}$, with l block zero matrices and $0 \in \mathbb{R}^{n \times n}$, along the diagonal. From linear algebra, $\mathbf{A}^l$ is zero for a strictly triangular matrix $\mathbf{A} \in \mathbb{R}^{l \times l}$ with dimension l [34], [35], [36]. We use this property for strictly upper triangular block matrix $K_{l,j}$ to avoid matrix inversion in (14), using the fact that $K_{l,j}^l = 0$ (l denotes the number of layers). Here

$$I - K_{l,j}^l = \left(I - K_{l,j} \right) \left(I + K_{l,j} + K_{l,j}^2 + \cdots + K_{l,j}^{l-1} \right) \quad (17)$$

implies that

$$\left(I - K_{l,j} \right)^{-1} = \left(I + K_{l,j} + K_{l,j}^2 + \cdots + K_{l,j}^{l-1} \right). \qquad (18)$$

Inserting (18) into (15) results in

$$\begin{aligned} \|F_{l,j}\| &= \left\| \left(I - K_{l,j} \right)^{-1} D_{l,j} \right\| \\ &\le \left\| \left(I + K_{l,j} + K_{l,j}^2 + \cdots + K_{l,j}^{l-1} \right) D_{l,j} \right\| \\ &\le \left(1 + \|K_{l,j}\| + \|K_{l,j}\|^2 + \cdots + \|K_{l,j}\|^{l-1} \right) \|D_{l,j}\| \end{aligned}$$
$$(19)$$

where the right-hand side of (19) is a geometric sum that can be rewritten as $(1 - \|K_{l,j}\|^{l-1})/(1 - \|K_{l,j}\|) \times \|D_{l,j}\|$. Therefore, if the RMC parameter $(1 - \|K_{l,j}\|^{l-1})/(1 - \|K_{l,j}\|) \times \|D_{l,j}\| < 1$, $\|F_{l,j}\|$ will be less than one. ∎

Note that because of norm properties in (19), the RMC criteria in corollary 1 are more conservative than the criteria presented in (15).

A. Nominal Stability and Convergence

For the additive model in (1), the nominal plant matrix results from the desired topography, $H_0 = H(\mathbf{g}_d)$. The nominal matrices are

$$D_{0_l} = \begin{bmatrix} T_0^h & \cdots & 0 \\ \vdots & \ddots & \vdots \\ 0 & \cdots & T_0^h \end{bmatrix}$$

$$K_{0_l} = \begin{bmatrix} 0 & T_0^{v_1} & \cdots & T_0^{v_{l-2}} & T_0^{v_{l-1}} \\ & & \ddots & \vdots & \vdots \\ & & & 0 & T_0^{v_1} \\ 0 & & \cdots & & 0 \end{bmatrix}. \qquad (20)$$

In this case, the following properties are true:

$$\|D_{0_l}\|_p = \|T_0^h\|_p \qquad (21a)$$

$$\|K_{0_l}\|_p \le \sum_{i=1}^{l-1} \|T_0^{v_i}\|_p \qquad (21b)$$

with $T_0^h = L_f^h - L_e^h H_0$ and $T_0^{v_i} = L_f^{v_i} - L_e^{v_i} H_0$. Equation (21b) has an equal sign for l_∞ norm of BCCB H_0 matrix.

Theorem 2: The system in (1) controlled by a nominal system representation of FO-SILC in (14) [or HO-SILC in (11)] is asymptotically stable (AS) for the nominal system if and only if

$$\rho\left(T_0^h\right) < 1 \qquad (22)$$

where ρ is the spectral radius.

Proof: To prove the nominal stability of (11), we need to prove the nominal representation of (14) is stable. The nominal form of the system given by (14) is AS if $\rho(F_{0_l}) < 1$, with $F_{0_l} = (I - K_{0_l})^{-1} D_{0_l}$. $(I - K_{0_l})^{-1}$ is a strictly upper triangular block matrix with block-diagonal matrices equal to I; therefore, the eigenvalues of F_{0_l} are equal to the eigenvalues of D_{0_l}. D_{0_l} is a block-diagonal matrix, and its spectral radius is equal to the spectral radius of the matrix T_0^h. Therefore, the nominal system is stable if $\rho(T_0^h) < 1$. ∎

The monotonic stability of the FO-SILC algorithm in (12) derives from (15); a nominal system representation of (14) is RMC stable using contraction mapping if $\|F_{0_l}\|_p < 1$. Using corollary 1, the conservative RMC criteria for the nominal system are defined as follows: $\text{RMC}_0 \triangleq (1 - \|K_{0_l}\|_P^{l-1})/(1 - \|K_{0_l}\|_p) \times \|T_0^h\|_p < 1$. Note that if $\|K_{0_l}\|_p \ll 1$, we can ignore $\|K_{0_l}\|_p^{l-1}$ compared with 1, especially at higher layers; as a result, RMC_0 can be approximate by a line, $\text{RMC}_0^{\text{app}} \triangleq \|K_{0_l}\|_p + \|D_{0_l}\|_p < 1$. The value $\text{RMC}_0 = 1$ is the boundary level for RMC stable regions of the nominal plant.

Remark 1: In order to avoid norm calculations of the high dimensional F_{0_l} or $K_{0_l} \in \mathbb{R}^{ln \times ln}$, the l_∞ norm can be used. Equation (21b) has an equality sign for l_∞, which reduces dimensionality in calculating matrix norms of $T_0^{v_i} \in \mathbb{R}^{n \times n}$ instead of $K_{0_l} \in \mathbb{R}^{ln \times ln}$.

B. Maximum AIU

In this section, we design the learning gain matrices in (8), such that HO-SILC remains stable for the maximum allowable interval uncertainty (AIU) added to the nominal plant. Altin et al. [19] formulated the iteration-varying system behavior as that of robustness under interval uncertainties with spatially invariant bounds for an FO-SILC system. In this section, we extend their results to HO-SILC systems.

Assume that the iteration-varying plant $H_{l,j} = H_0 + \Delta H_{l,j}$ is an interval matrix, and $\Delta H_{l,j}$ is additive uncertainty of the nominal plant. In order to quantify the maximum amount of allowable uncertainty, we define the uncertainty radius as $\Delta H_r \triangleq (\overline{H} - \underline{H})/2$. In general, ensuring the asymptotic and monotonic stability in (22) and (15) for all $H_{l,j} \in H^I$ is a difficult problem [19], [37]. The goal here is to find the maximum AIU, r_{AIU}, such that the RMC criteria in (16) are guaranteed for all $\|\Delta H_{l,j}\| < r_{\text{AIU}}$. We can solve this problem by ensuring the maximum amount of uncertainty in the system remains smaller than r_{AIU} at all iterations. In other words, if the learning filters in (9) are designed, such that $\|\Delta H_r\| < r_{\text{AIU}}$, we can ensure $\|\Delta H_{l,j}\| < r_{\text{AIU}}$ for all iterations and layers. Iteration-varying matrices in (11) can be written as $T_{l,j}^h = T_0^h - L_e^h \Delta H_{l,j}$ and $T_{l,j}^{v_i} = T_0^{v_i} - L_e^{v_i} \Delta H_{l,j}$. We can

decompose the rest of the matrices as in (23), (24a), and (24b), as shown at the bottom of the next page. Inserting (17) and (23) into (14), F can be decomposed as the following:

$$F_{l,j} = \left(I + \left(K_{0_l} + \Delta K_{l,j}\right) + \cdots + \left(K_{0_l} + \Delta K_{l,j}\right)^{l-1}\right)$$
$$\times \left(D_{0_l} + \Delta D_{l,j}\right)$$
$$= \left(\mathbf{a}_{0_l} + \mathbf{a}_{1_l}\Delta K_{l,j} + \mathbf{a}_{2_l}\Delta K_{l,j}^2 + \cdots\right)$$
$$\times \left(D_{0_l} + \Delta D_{l,j}\right) \qquad (25a)$$

$$\mathbf{a}_{0_l} = I + K_{0_l} + K_{0_l}^2 + \cdots + K_{0_l}^{l-1} \qquad (25b)$$

$$\mathbf{a}_{1_l} = I + 2K_{0_l} + 3K_{0_l}^2 + \cdots + (l-1)K_{0_l}^{l-2}, \quad l \geq 2 \qquad (25c)$$

$$\mathbf{a}_{2_l} = I + 3K_{0_l} + 6K_{0_l}^2 + 10K_{0_l}^3$$
$$+ \cdots + \frac{(l-1)(l-2)}{2}K_{0_l}^{l-3}, \quad l \geq 3. \qquad (25d)$$

Ignoring the higher-order terms for small model uncertainties around the nominal plant ($\Delta H^n \simeq 0$ for $n > 2$)

$$F_{0_l} = \mathbf{a}_{0_l}D_{0_l}$$
$$\Delta F_{l,j} \simeq \left(\mathbf{a}_{1_l}\Delta K_{l,j} + \mathbf{a}_{2_l}\Delta K_{l,j}^2\right)D_{0_l}$$
$$+ \left(\mathbf{a}_{0_l} + \mathbf{a}_{1_l}\Delta K_{l,j}\right)\Delta D_{l,j}. \qquad (26)$$

Theorem 3: Given the learning matrices designed for the nominal plant H_0, such that the nominal system is AS ($\rho(T_0^h) < 1$), the iterative system in (1), controlled by the FO-SILC in (14), remains AS if

$$\|\Delta H_r\|_p < r_{\text{AIU}}^{\text{Asym}}, \quad r_{\text{AIU}}^{\text{asym}} = \frac{-\mu_1 + \sqrt{\mu_1^2 + 4\frac{\mu_2}{\|P\|_\infty}}}{2\mu_2} \qquad (27)$$

where μ_1 and μ_2 are positive scalars that are a function of the learning filters and nominal plant

$$\mu_1 = 2\theta_1 \langle F_{0_l}\rangle_p, \quad \mu_2 = 2\theta_2 \langle F_{0_l}\rangle_p + \theta_1^2 \qquad (28a)$$

$$\theta_1 = \langle \mathbf{a}_{0_l}\rangle_p \langle L_e^h\rangle_p + \langle \mathbf{a}_{1_l}\rangle_p \langle T_0^h\rangle_p \sum_{i=1}^{l-1}\langle L_e^{v_i}\rangle_p$$

$$\theta_2 = \langle \mathbf{a}_{1_l}\rangle_p \langle L_e^h\rangle_p \sum_{i=1}^{l-1}\langle L_e^{v_i}\rangle_p + \langle \mathbf{a}_{2_l}\rangle_p \langle T_0^h\rangle_p \left(\sum_{i=1}^{l-1}\langle L_e^{v_i}\rangle_p\right)^2 \qquad (28b)$$

where $\langle \mathbf{B}\rangle_p \triangleq \max(\|\mathbf{B}\|_p, \|\mathbf{B}^T\|_p)$ for an arbitrary square matrix $\mathbf{B}$ in l_p norm. In (27), P is a symmetric and positive definite matrix that satisfies the Lyapunov stability of the nominal plant [10]

$$F_{0_l}^T P F_{0_l} - P = -I. \qquad (29)$$

Proof: Assume the FO-SILC in (14) is AS for the nominal plant; from Lyapunov stability, there exists a positive definite $P > 0$, such that (29) is satisfied. The iteration-varying FO-SILC is AS in the Lyapunov sense, if the following inequality is satisfied with the same P from (29):

$$F_{l,j}^T P F_{l,j} - P < 0, \quad l = 1, 2, \ldots, L, \; j = 1, 2, \ldots, J. \qquad (30)$$

This article has been accepted for inclusion in a future issue of this journal. Content is final as presented, with the exception of pagination.

8

IEEE TRANSACTIONS ON CONTROL SYSTEMS TECHNOLOGY

Defining $\|\Delta H\|_p \triangleq \max_{l,j}(\|\Delta H_{l,j}\|_p)$, the following induced norms hold for $\Delta K_{l,j}$ and $\Delta D_{l,j}$:

$$\left\|\Delta D_{l,j}\right\|_p \le \left\|L_e^h\right\|_p \|\Delta H\|_p \tag{31a}$$

$$\left\|\Delta K_{l,j}\right\|_p \le \left(\sum_{i=1}^{l-1} \|L_e^{v_i}\|_p\right)\|\Delta H\|_p. \tag{31b}$$

Inserting (26) and (29) into (30) and taking the norm of both sides, we have the following:

$$\left(F_{0_l} + \Delta F_{l,j}\right)^T P\left(F_{0_l} + \Delta F_{l,j}\right) - P < 0$$

$$\xrightarrow{\|\cdot\|_p} 2\langle F_{0_l}\rangle_p \langle \Delta F_{l,j}\rangle_p + \langle \Delta F_{l,j}\rangle_p^2 < \frac{1}{\|P\|_p}. \tag{32}$$

Using (31a) and (31b) and taking l_p norm of both sides of (26), we have the following:

$$\langle \Delta F_{l,j}\rangle_p \le \theta_2 \langle \Delta H\rangle_p^2 + \theta_1 \langle \Delta H\rangle_p \tag{33}$$

where θ_1 and θ_2 are defined in (28b). Neglecting higher-order terms for small model uncertainties ($\|\Delta H\|_p^n \approx 0, \forall n \ge 3$), (32) can be simplified to a quadratic equation for $\langle \Delta H\rangle_p$

$$\mu_1 \langle \Delta H\rangle_p + \mu_2 \langle \Delta H\rangle_p^2 - \frac{1}{\|P\|_p} < 0 \tag{34}$$

which is negative when $\langle \Delta H\rangle_p < (-\mu_1 + (\mu_1^2 + 4(\mu_2/\|P\|_\infty))^{1/2})/(2\mu_2)$. μ_1 and μ_2 are defined in (28a) and (28b). Therefore, $r_{\text{AIU}}^{\text{asym}} = (-\mu_1 + (\mu_1^2 + 4(\mu_2/\|P\|_\infty))^{1/2})/(2\mu_2)$. Note that if (34) holds, then (32) is true, not vice versa. ∎

Note that assuming bounded model uncertainty, Theorem 3 provides sufficient condition for BIBO stability of the HO-SILC in (11).

Theorem 4: Given the learning matrices are designed, such that the nominal system is RMC stable ($\|F_{0_l}\| < 1, \forall l$), the iterative additive process in (1), controlled by the FO-SILC in (14), remains robustly monotonically stable if

$$\|\Delta H_r\|_p < r_{\text{AIU}}^{\text{mono}}, \quad r_{\text{AIU}}^{\text{mono}} = \frac{-\mu_1 + \sqrt{\mu_1^2 + 4\frac{\mu_2}{\|P_s\|_p}}}{2\mu_2} \tag{35}$$

where P_s is a positive definite matrix that satisfies the following equation:

$$S_{0_l}^T P_s S_{0_l} - P_s = -I, \quad S_{0_l} = \begin{bmatrix} 0 & F_{0_l}^T \\ F_{0_l} & 0 \end{bmatrix}. \tag{36}$$

Proof: As it was explained earlier in (15), monotonic stability of (14) is achieved if $\|F_{l,j}\|_p < 1$. If the l_2 norm is used, then $\|F_{l,j}\|_2 = \bar{\sigma}(F_{l,j})$. The maximum singular value of a matrix (here, $F_{l,j}$) is defined as follows:

$$\bar{\sigma}(F_{l,j}) = \sqrt{\rho\left(F_{l,j}^T F_{l,j}\right)}. \tag{37}$$

Equation (37) implies if $\rho(F_{l,j}^T F_{l,j}) < 1$, then $\bar{\sigma}(F_{l,j}) < 1$. In other words, the maximum singular value problem for MC can be solved equivalently as an eigenvalue problem. Following the same steps as (30)–(34), maximum allowable uncertainty of the nominal plant for MC of (14) can be achieved [10]. Note that the eigenvalues of $F^T F$ are equal to the eigenvalues of S

$$S_{l,j} = S_{0_l} + \Delta S_{l,j}, \quad S_{l,j} = \begin{bmatrix} 0 & F_{l,j}^T \\ F_{l,j} & 0 \end{bmatrix}$$

$$\Delta S_{l,j} = \begin{bmatrix} 0 & \Delta F_{l,j}^T \\ \Delta F_{l,j} & 0 \end{bmatrix}. \tag{38}$$

Assume the FO-SILC in (14) is monotonically stable for the nominal plant; from Lyapunov stability, there exists a positive definite $P_s > 0$, such that (36) holds. Similarly, the iteration-varying FO-SILC is monotonically stable based on the Lyapunov stability ($\rho(S_{l,j}) = \bar{\sigma}(F_{l,j}) < 1$), if the following inequality holds with the same P_s from (36):

$$S_{l,j}^T P_s S_{l,j} - P_s < 0 \quad \forall l \; \& \; j. \tag{39}$$

Inserting (38) into (39) and using (36), we have the following:

$$S_{0_l}^T P_s \Delta S_{l,j} + \Delta S_{l,j}^T P_s S_{0_l} + \Delta S_{l,j}^T P_s \Delta S_{l,j} < I. \tag{40}$$

Given $\|S_{0_l}\|_p = \langle F_{0_l}\rangle_p$ and $\|\Delta S_{l,j}\|_p = \langle \Delta F_{l,j}\rangle_p$ and taking l_p norm of both sides of (40), we have the following:

$$2\langle F_{0_l}\rangle_p \langle \Delta F_{l,j}\rangle_p + \langle \Delta F_{l,j}\rangle_p^2 < \frac{1}{\|P_s\|_p}. \tag{41}$$

Using (26) and (33), (41) simplifies to a quadratic equation for $\|\Delta H\|_p$

$$\mu_1 \|\Delta H\|_p + \mu_2 \|\Delta H\|_p^2 - \frac{1}{\|P_s\|_p} < 0 \tag{42}$$

which is negative when $\|\Delta H\|_p < (-\mu_1 + (\mu_1^2 + 4(\mu_2/\|P_s\|_p))^{1/2})/(2\mu_2)$. μ_1 and μ_2 are defined in (28a) and (28b). Therefore, $r_{\text{AIU}}^{\text{mono}} = (-\mu_1 + (\mu_1^2 +$

$$D_{l,j} = D_{0_l} + \Delta D_{l,j}, \quad K_{l,j} = K_{0_l} + \Delta K_{l,j}, \quad F_{l,j} = F_{0_l} + \Delta F_{l,j} \tag{23}$$

$$\Delta D_{l,j} = -L_e^h \begin{bmatrix} \Delta H_{l-1,j} & \cdots & 0 \\ \vdots & \ddots & \vdots \\ 0 & \cdots & \Delta H_{0,j} \end{bmatrix} \tag{24a}$$

$$\Delta K_{l,j} = -\begin{bmatrix} 0 & L_e^{v_1}\Delta H_{l-2,j+1} & L_e^{v_2}\Delta H_{l-3,j+1} & \cdots & L_e^{v_{l-1}}\Delta H_{0,j+1} \\ & 0 & L_e^{v_1}\Delta H_{l-3,j+1} & \cdots & L_e^{v_{l-2}}H_{0,j+1} \\ \vdots & & \ddots & & \vdots \\ & & & 0 & L_e^{v_1}\Delta H_{0,j+1} \\ 0 & & \cdots & & 0 \end{bmatrix} \tag{24b}$$
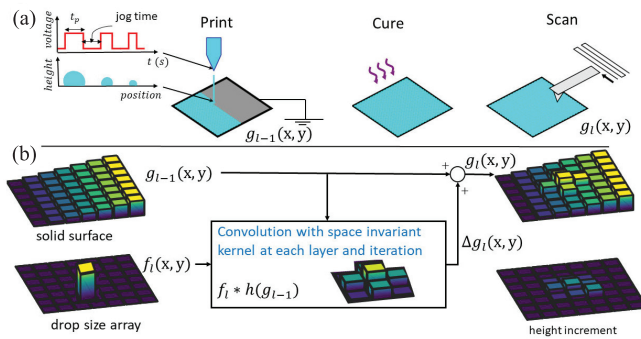
Fig. 3. Heightmap evolution process. (a) Schematic of an e-jet printer: controlled device fabrication follows the print-cure-scan cycle. High-voltage pulse actuation is applied at the nozzle tip to eject a droplet of material with droplet volume related to pulsewidth. (b) Evolution of the solid surface topography as a heightmap signal is modeled as the integration of a convolution of input f with kernel h. h is a function of local variation in g for each pixel in g. Subscript l represents the layer index.
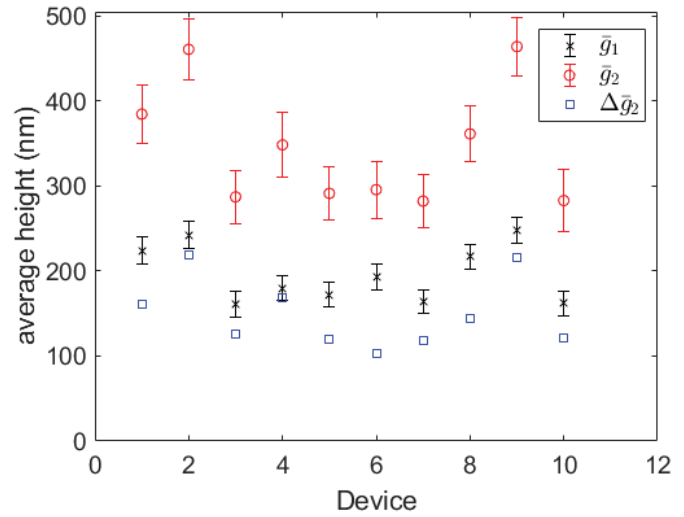

Fig. 4. Experimental data for deposition of Loctite 3526: $\bar{g}_1$, $\bar{g}_2$, and $\Delta\bar{g}_2$ are average height of layers 1 and 2, and incremental height at layer 2 over a 7×9 discretized domain.

$4(\mu_2/\|P_s\|_p))^{1/2})/(2\mu_2)$. Note that if (42) is true, then (41) is true, not vice versa. ∎

Remark 2: By direct substitution of S_{0_l} into (36), it is evident that $P_s = \mathrm{diag}(P, P)$ and $\|P_s\|_p = \|P\|_p$, which results in $r_{\mathrm{AIU}}^{\mathrm{mono}} = r_{\mathrm{AIU}}^{\mathrm{asym}}$. We denote $r_{\mathrm{AIU}} \triangleq r_{\mathrm{AIU}}^{\mathrm{mono}} = r_{\mathrm{AIU}}^{\mathrm{asym}}$, as an estimate on the maximum AIU.

Remark 3: The special structure of K_{0_l} in (20) results in $\|K_{0_l}\|_1 = \|K_{0_l}\|_\infty$.

VI. SYSTEM MODEL AND SIMULATION SETUP

In this section, we apply the proposed HO-SILC framework to a simulation study using different models of an e-jet printing process. E-jet achieves material deposition using an electrostatic field, allowing for high-resolution deposition and material diversity. Drop-on-demand printing is achieved using synchronized substrate motion (jog time) and high-voltage pulses applied to the nozzle tip of an e-jet printer. Varying the rectangular wave pulsewidth (while holding all other printing parameters constant) allows for variation in printed droplet size, as shown in Fig. 3(a). The simulation assumes a known relationship between pulsewidth and droplet size. Controlled topography evolution requires output measurements. As such, the printing process follows a print-cure-scan cycle to obtain the necessary measurement data [see Fig. 3(a)]: 1) print an array of droplets of prescribed sizes at discretized coordinates; 2) cure (solidify) the droplets; and 3) scan the solid surface to obtain heightmap measurements of topography [29].

A. Model Approximation

In this section, we explore three methods to estimate the spreading model of liquid inks, θ, such that $\|g_{l+1} - \phi(g_l, f_{l+1})\hat{\theta}\|$ is minimized, where $\hat{\theta}$ is an estimation of the true θ, and $\phi(g_l, f_{l+1})$ is a nonlinear transformation between g_{l+1} and θ. Note that a linearized form of ϕ can be used for control design. Fig. 4 shows the experimental data from [28] that are used for model development and validation. We use eight devices (63 nodes $\times 8$) in Fig. 4 for training and two devices to test the accuracy of the model of constrained linear regression (CLR) and convolutional recurrent neural network (CRNN) models in the next sections. The variables g_1, g_2, and Δg_2 define material height at layer 1 and layer 2, and the

incremental height at layer 2. To capture the merging behavior of Loctite 3526 with itself, we assume a base layer of material and start the system identification using the input signal at layer 2 (f_2). The layers are printed using a 2-D pseudorandom binary sequence (PRBS) pulsewidth signal (described in [28]), with a 35×45-μm spatial plane discretized into 7×9 grids for a 5-μm droplet-to-droplet distance known as pitch.

1) Constrained Linear Regression: The sequence of material addition in multilayer structures using a constrained regression model is developed in [28]

$$g_{l+1}(x, y) = (g_l * h_g)(x, y) + (f_{l+1}^p * h_f)(x, y). \quad (43)$$

In (43), $h_f \in \mathbb{R}^{5\times 5}$ is the discrete impulse response to the current layer input, while $h_g \in \mathbb{R}^{5\times 5}$ is the discrete impulse response to the previous layer output. $f_{l+1}^p \in \mathbb{R}^{n_x \times n_y}$ is the pulsewidth signal at layer l. Assuming rotational symmetry of liquid droplets in [28], h_f and h_g are defined by only six parameters. To find the unknown $\theta^{LR} = [h_f^T h_g^T]^T \in \mathbb{R}^{12\times 1}$, the design matrix $\phi(g_l, f_{l+1}^p) \in \mathbb{R}^{n\times 12}$ is constructed using the conv2($\cdot$) function in MATLAB, and the optimization, $\|g_{l+1} - \phi(g_l, f_{l+1}^p)\hat{\theta}^{LR}\|$, is solved using the built-in solver lsqlin() in MATLAB. Assuming volume conservation from layer to layer, h_g has only one nonzero element at the center, $h_g(3, 3) = 1$. For Loctite 3526, h_f is calculated as follows:

$$h_f = \begin{bmatrix} 0.09 & 0.09 & 0.21 & 0.09 & 0.09 \\ 0.09 & 0.21 & 0.38 & 0.21 & 0.09 \\ 0.21 & 0.38 & 0.71 & 0.38 & 0.21 \\ 0.09 & 0.21 & 0.38 & 0.21 & 0.09 \\ 0.09 & 0.09 & 0.21 & 0.09 & 0.09 \end{bmatrix} \left(\frac{\mathrm{nm}}{\mathrm{ms}}\right).$$

2) LPV Model: The linear parameter-varying (LPV) model in [29] is described using the following 2-D convolution equation:

$$g_l(x, y) = g_{l-1}(x, y) + \sum_{\substack{m\in\mathbb{Z}_{n_x} \\ n\in\mathbb{Z}_{n_y}}} h_{l-1}^{(m,n)}(x - m, y - n)$$

$$* f_l^{\mathrm{LPV}}(m, n). \quad (44)$$

This article has been accepted for inclusion in a future issue of this journal. Content is final as presented, with the exception of pagination.

10

IEEE TRANSACTIONS ON CONTROL SYSTEMS TECHNOLOGY

Following the model of [29] and assuming the relationship between the applied pulsewidth and droplet volume is known, we take a 2-D array of cube roots of drop volumes to be the input, denoted by f_l^{LPV}. The variable $h_{l-1}^{(m,n)}$ describes the spreading behavior of a printed droplet on the neighboring coordinates for an input signal with magnitude one applied at coordinate (m, n) and layer $l - 1$. Spreading behavior of the printed droplet depends on surface energy and topography of the substrate, as well as surface tension, viscosity, and density of the printing material [30].

The dependence of $h_l^{(m,n)}$ on existing topography g_l is modeled using the multivariate regression method proposed in [29]. In this method, numerical simulations of droplets spreading on nonflat surfaces are computed for equilibrium contact angles associated with a specific material/substrate combination: 30° for the ink (Loctite 3526) used in this simulation. Subsequently, an ordinary least squares multivariate linear regression is performed, where the elements from each 3×3 pixel crop of the heightmap g are the predictor variables, and the elements from each measured 3×3 pixel impulse response h are the response variables. The fit regression model is used to evaluate the spatially varying impulse response (method M2 in [29]), $h_{l-1}(x, y)$, for the 3×3 pixel crop of the heightmap g_l centered at pixel coordinates (x, y). Taking the average of $h_{l-1}(x, y)$ over all spatial coordinates $(x \in \mathbb{Z}_{n_x}, y \in \mathbb{Z}_{n_y})$ results in a spatially invariant impulse response (method M3 in [29]), h_{l-1} in Fig. 5(a) and (b). Note that the spatially invariant approximation results in a less accurate model than the spatially varying model; however, the spatially invariant plant matrix is BCCB. Importantly, the magnitude of $\mathbf{g}_l$ does not affect the impulse response; only the local variation in $\mathbf{g}_l$ affects h_l. The nominal model, h_0, is calculated using the regression model's prediction of spreading on a reference topography, g_d, denoted as $h_0 = h(g_d)$, and shown in Fig. 5(b) for a flat reference topography used in this example. In contrast, an example of an impulse response for a nonflat surface is shown in Fig. 5(a). Impulse response bounds are calculated from the supremum and infimum of each element of h_l determined by simulating the deposition of printed material on multiple topographies of the same substrate material.

3) Convolutional Recurrent Neural Network: Layer-to-layer material addition using a CRNN model is developed in [25]. This model considers the surface tension of liquid droplets, parameterized by κ known as the flowability parameter, that causes the droplets to move from higher to lower height locations of nearby pixels

$$\mathbf{y}_l^t = \mathbf{y}_l^{t-1} - D\sigma\left(K D^T \mathbf{y}_l^{t-1}\right) + W_u \mathbf{u}_l^t \tag{45a}$$

$$\mathbf{g}_l(i) = \ln\left(\gamma + e^{y_l^n(i)+v_0}\right), \quad i, t \in [1, n] \tag{45b}$$

$$\mathbf{y}_l^0 = \mathbf{g}_{l-1} \tag{45c}$$

where $\mathbf{y}_l^t \in \mathbb{R}^{n \times 1}$ defines the network internal states at layer l and time step t, which refer to the unmeasured material addition states during in-layer deposition of a single droplet in liquid form. Also, $\mathbf{g}_l \in \mathbb{R}^{n \times 1}$ is the measured topography of layer l once the material has been UV cured. In addition,
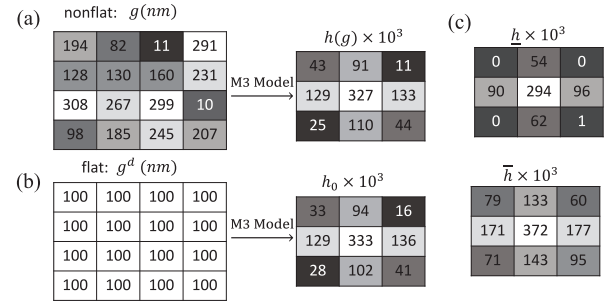

Fig. 5.   Topography-dependent impulse response. The estimated impulse response is spatial-invariant (method M3 of [29]), meaning that it is the same for every spatial coordinate of $g(x, y)$. Note that the estimated impulse response is iteration-varying. (a) Effect of a nonflat surface. At left is a 4×4 pixel of a random g signal to show the effect of significant surface variation. At right is the 3×3 model's corresponding impulse response (h). (b) Effect of flat surface. At left is a 4×4 pixel of a flat reference topography signal. At right is the 3×3 model's corresponding nominal impulse response (h_0). (c) Upper and lower bounds of h, $\overline{h}$, and $\underline{h}$, such that $\underline{h} \preceq h \preceq \overline{h}$.

$\mathbf{u}_l^t \in \mathbb{R}^{n \times 1}$ is the ratio of the size of the deposited droplet at time step t to the maximum droplet size. The input signal of the entire layer is given by $\mathbf{f}_l^{\text{CRNN}} = \sum_{t=1}^n \mathbf{u}_l^t$. Note that we assume the relationship between the applied pulsewidth and the droplet size is known. $D \in \mathbb{R}^{n \times n_l}$ is the incidence matrix that transforms the height profile of all discretized grids into height differences or links. $D(i, j)$ is either 1 or -1 for nearby pixels, and zero for nodes that are far away in 2-D space.

We define the number of links between the nodes as n_l, with $K = \kappa I \in \mathbb{R}^{n_l \times n_l}$ constructed as a diagonal matrix with nonzero elements along the diagonal that captures the material flow along each link. In 45a, $\sigma(l_t)$ represents the leaky soft threshold function that is set to zero if the effective flow at each time step is smaller than a threshold value ϵ, $l_t = K D^T \mathbf{y}_l^{t-1} < \epsilon$. The matrix $W_u \in \mathbb{R}^{n \times n}$ is a BCCB matrix associated with the convolution kernel $b \in \mathbb{R}^{5 \times 5}$, such that $W_u \mathbf{u}_l^t = v(b * u_l^t)$. Note that, b is the kernel related to the spreading behavior of the largest droplet. From the definition of $\mathbf{u}_l^t$, the elements of the input signal f_l^{CRNN} are bounded between $0 \leq f_l^{\text{CRNN}}(i) \leq 1$. Finally, v_0 is the material shrinkage parameter due to UV curing, and γ is a nonnegative scalar that ensures that the output heightmap remains nonnegative.

To derive the CRNN model, the unknown parameters of $\theta^{\text{CRNN}} = [\epsilon, b, \kappa, \gamma, v_0]$ for the printing material of interest (e.g., Loctite 3526) are calculated from experimental data using the steps described in [25]

$$\epsilon = 6.66, \quad \kappa = 1.12 \times 10^{-5}$$

$$\gamma = 1.014, \quad v_0 = 56.88 \text{ (nm)}$$

$$b = \begin{bmatrix} -6.77 & -9.99 & 45.58 & -9.99 & -9.98 \\ 23.97 & 28.03 & 58.74 & 2.72 & -1.17 \\ 32.68 & 36.76 & 100.0 & 45.12 & 39.80 \\ 7.60 & 1.08 & 39.91 & -6.38 & 3.30 \\ 24.35 & 6.66 & 26.95 & 0.91 & 20.98 \end{bmatrix} \text{ (nm)}.$$

4) Model Validation: To evaluate the performance of the different modeling approaches, experimental data from printed samples of Loctite 3526 are used to derive the difference between the measured and predicted output topographies. The

This article has been accepted for inclusion in a future issue of this journal. Content is final as presented, with the exception of pagination.

AFKHAMI et al.: ROBUST HO-SILC FOR AM SYSTEMS   11
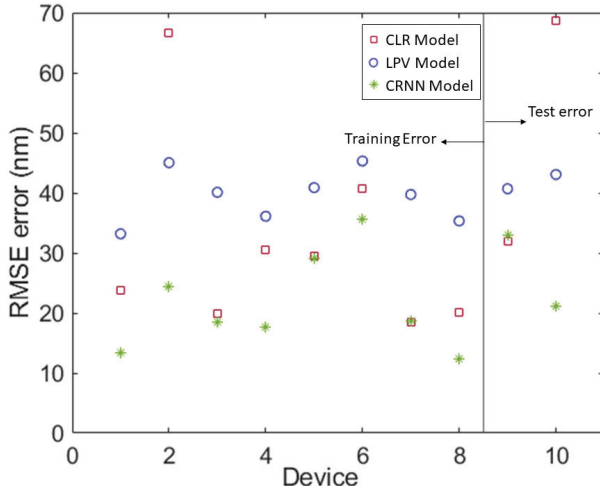

Fig. 6. Performance comparison: experimental data from printing Loctite 3526 is used to compare the different modeling approaches. The error is computed as $e = g_2^{\exp} - \hat{g}_2$, where $\hat{g}_2$ is the prediction of $g_2^{\exp}$ using different modeling approaches. Note that $\hat{g}_2$ is a function of $g_1^{\exp}$ and the input signal at the second layer.

error metric is defined as $\|g_2^{\exp} - \phi(g_1^{\exp}, f_{l+1}^{\exp})\hat{\theta}\|_2^2$, where $g^{\exp}$ refers to the measured experimental values, $f^{\exp}$ is the derived input signal, and $\hat{\theta}$ is the model from each method, respectively. Note that the input signal for each model is different.

The results in Fig. 6 illustrate that the CRNN model that considers surface material flowability is more accurate than the other models. However, the CRNN model is nonlinear and computationally expensive; thus, it is well suited to represent the *true* system in the simulation case studies, but cannot be used for linear control design. As a comparison, the linear LPV and CLR models are $\approx 50\%$ computationally faster than the CRNN model. The LPV model captures the wetting nonlinearity due to nonflatness of the previous layer and yet still maintains access to linear control. However, the LPV model does not capture droplet-to-droplet effects due to surface tension, since the model assumes that the droplets are placed far away from each other. In this approach, multiples passes are required to form a thin film by depositing droplets spatially distanced from each other and curing the material between passes to avoid coalescence effects. Since the experimental layers in Fig. 4 are fabricated in one printing pass, the LPV model does not capture unmodeled nonlinearities due to surface tension of the droplets for thin-film formation. Alternatively, the CLR model captures droplet-to-droplet effects within the h_f matrix. However, this model does not take previous layer topography into consideration, thus ignoring an important consideration for error propagation from layer to layer. In this work, we consider the use of the LPV and linearized CRNN models to develop the controllers. We will use the nonlinear CRNN model as the *true* system within the simulation case studies.

5) Lifted Conversion: The systems defined in (44) can be transferred into the lifted form through the use of a vectorization operator defined in Section II-A. A full description of the lifted-domain conversion can be found in [18]. For brevity, we present the lifted form of (44) in the

following equation:

$$g_l = g_{l-1} + H(g_{l-1})f_l^{\text{LPV}}, \quad H \in H^I \quad (46)$$

with $\quad f_l^{\text{LPV}} \triangleq \nu(f_l^{\text{LPV}}(x, y)) \in \mathbb{R}^{n \times 1}$, and $g_l \triangleq \nu(g_l(x, y)) \in \mathbb{R}^{n \times 1}$.

To convert the CRNN model in (45) to the lifted domain and enable access to linear control, we consider a linearized form of the CRNN model around an equilibrium point $(\mathbf{f}_e, \Delta \mathbf{g}_e)$:

$$\Delta g_l = H_J \mathbf{f}_l^{\text{CRNN}} + \Delta g_e - H_J \mathbf{f}_e \quad (47)$$

where $H_J \in \mathbb{R}^{n \times n}$ is the Jacobian matrix at the equilibrium point. Note that the Jacobian matrix, H_J, is not BCCB; therefore, DFT calculations in (9) and (10) are not possible for the linearized CRNN model. More details on Jacobian and equilibrium point calculations are presented in the Appendix.

In addition to Assumptions A_1–A_3, the following assumptions are considered for the CRNN or LPV models in (47) and (46).

1) A_4: The heightmap increments using the LPV model obey scalar multiplication and linear superposition. Therefore, the model described in (46) does not capture drop coalescence effects.

2) A_5: The CRNN model based on [25] is geometrically independent, and the Jacobian matrix in (47) is iteration-invariant.

Assumption A_4 is a major assumption of the additive model in (46) that simplifies the system dynamics for control design. Many AM processes exhibit coalescence/surface effects that preclude linear superposition [29]. For instance, in a physical AM deposition process, depositing twice the volume of material does not cause the incremental heightmap to double. We capture these nonlinearities through model uncertainty applied to the plant model in (45). The CRNN model, on the other hand, considers these surface effects by implementing a graph structure with n_l links between nodes that incorporate the effect of the liquid material flow between nearby droplets. Assumption A_5 implies that the model parameters of the ink are generalizable to any geometry for the CRNN model in (45) based on the incorporation of a physical understanding of mass conservation during height evolution. When we linearize the CRNN model around an equilibrium point, the resulting Jacobian matrix is a constant matrix.

B. Simulation Study

For this simulation, a multilayered structure with $L = 6$ layers is considered [Fig. 2(a)]. The reference device structure has the reference height map, Δg^d, given in Fig. 2(a) with 100-nm layer heights for all layers, which is uniform except for the two outer rings of pixels that are reduced by half to better represent material drop-off at the edges. Each layer is printed in a single printing pass on top of a cured surface. For the first (bottom) layer in the simulation, the underlying surface, $(l = 0)$, is assumed to be a prelayer of cured printing material, so that the first-layer surface interactions with other substrate materials need not be considered. In e-jet printing, droplet volume has a standard variation of 25% over a wide range of droplet

This article has been accepted for inclusion in a future issue of this journal. Content is final as presented, with the exception of pagination.

12   IEEE TRANSACTIONS ON CONTROL SYSTEMS TECHNOLOGY

TABLE I
DESIGN METHODOLOGY FOR THE LPV MODEL, $\beta = 0.0$

	l_2 norm							l_∞ norm						
α	$\|K_{0_L}\|$	$\|T_0^h\|$	RMC_0	RMC^{app}	$\|F_{0_L}\|$	$\|P\|$	r_{AIU}	$\|K_{0_L}\|$	$\|T_0^h\|$	RMC_0	RMC_0^{app}	$\|F_{0_L}\|$	$\|P\|$	r_{AIU}
0.00	0.00	0.099	0.099	0.099	0.099	1.01	0.561	0.00	0.190	0.190	0.190	0.189	1.022	0.232
0.25	0.308	0.099	0.144	0.408	0.099	1.01	0.442	0.598	0.189	0.459	0.788	0.210	1.024	0.136
0.50	0.849	0.099	0.450	0.948	0.099	1.01	0.345	1.742	0.188	12.13	1.931	0.241	1.028	0.077
0.75	1.917	0.099	10.24	2.016	0.099	1.01	0.243	4.311	0.185	1552.7	4.497	0.295	1.032	0.034
1.0	4.216	0.099	735.24	4.316	0.099	1.01	0.103	9.822	0.176	176100	9.998	0.394	1.038	0.012

TABLE II
DESIGN METHODOLOGY FOR THE LPV MODEL, $\beta = 0.25$

	l_2 norm							l_∞ norm						
α	$\|K_{0_L}\|$	$\|T_0^h\|$	RMC_0	RMC^{app}	$\|F_{0_L}\|$	$\|P\|$	r_{AIU}	$\|K_{0_L}\|$	$\|T_0^h\|$	RMC_0	RMC_0^{app}	$\|F_{0_L}\|$	$\|P\|$	r_{AIU}
0.0	0.111	0.088	0.099	0.199	0.098	1.009	0.545	0.216	0.167	0.213	0.383	0.192	1.021	0.198
0.25	0.301	0.088	0.126	0.389	0.098	1.009	0.475	0.670	0.167	0.476	0.837	0.201	1.022	0.135
0.50	0.837	0.088	0.386	0.926	0.098	1.009	0.376	1.781	0.166	11.86	1.947	0.227	1.024	0.079
0.75	1.893	0.088	8.519	1.981	0.098	1.009	0.274	4.257	0.163	1268.9	4.42	0.280	1.027	0.037
1.0	4.141	0.088	587.9	4.229	0.098	1.009	0.127	9.491	0.154	125870	9.645	0.379	1.032	0.014

TABLE III
DESIGN METHODOLOGY FOR THE LPV MODEL, $\beta = 0.75$

	l_2 norm							l_∞ norm						
α	$\|K_{0_L}\|$	$\|T_0^h\|$	RMC_0	RMC^{app}	$\|F_{0_L}\|$	$\|P\|$	r_{AIU}	$\|K_{0_L}\|$	$\|T_0^h\|$	RMC_0	RMC_0^{app}	$\|F_{0_L}\|$	$\|P\|$	r_{AIU}
0.0	0.148	0.081	0.095	0.229	0.092	1.008	0.562	0.353	0.152	0.236	0.506	0.190	1.019	0.183
0.25	0.297	0.081	0.115	0.378	0.092	1.008	0.501	0.799	0.152	0.601	0.952	0.199	1.019	0.128
0.50	0.829	0.081	0.347	0.911	0.092	1.008	0.400	1.803	0.151	11.49	1.954	0.218	1.021	0.084
0.75	1.876	0.081	7.47	1.957	0.092	1.008	0.298	4.210	0.148	1085.7	4.359	0.255	1.022	0.044
1.0	4.083	0.081	497.8	4.164	0.092	1.008	0.145	9.233	0.139	97126	9.373	0.342	1.026	0.017

sizes [38]. Therefore, a normally distributed white noise is added to the input signal of both models [linearized CRNN in (47) and LPV in (46)]. For example, for the LPV model, a normally distributed white noise with a variance of 0.25 μm is added to the input signal, such that $\Delta \mathbf{g}_{l,j} = H_{l-1,j} \mathbf{f}_{l,j}^{LPV} \circ (\mathbf{1}_{n \times 1} + \mathcal{N}(0, 0.25^2)_{n \times 1})$, where $\mathbf{1}$ is a vector of ones. The input will be constrained to nonnegative values to ensure an additive process.

It is important to note that the input of the first iteration at the first layer is zero, $\mathbf{f}_{1,1} = \mathbf{0}$, implying that there is no prior knowledge of the appropriate input. This results in no material being deposited during the first iteration of the first layer. However, the input of the first device at higher layers, $l \geq 2$, comes from the last device in the previous layer, such that $\mathbf{f}_{l,1} = \mathbf{f}_{l-1,J}$, where $J = 30$ is the total number of iterations.

The LPV model in (46) is used to design the HO-SILC learning filters in (9), and the results are shown in Figs. 7 and 8(a) and (b) and Tables I–III. The linearized CRNN model in (47) is used to design the learning filters in (8), and the results are shown in Fig. 9. In the absence of the experimental data, the error is calculated from the difference between the desired and simulated height increment predicted by the nonlinear CRNN model in Section VI-A3. The plant matrix bounds for the LPV model, $\underline{H}$ and $\overline{H}$, are calculated from $\underline{h}$ and $\overline{h}$ in Fig. 5(c) by the BCCB construction method described in Section II-B.

For Loctite 3526, the nominal impulse response and the invariant bounds shown in Fig. 5(c) and the corresponding norms are as follows: $\|\Delta H_0\|_2 = 0.411$, $\|\Delta H_r\|_2 = 0.118$, and $\|\Delta H_r\|_\infty = 0.123$. We set $q = 1$, $r = 0.01$, and $s = 0.09$ and look for appropriate α and β, such that
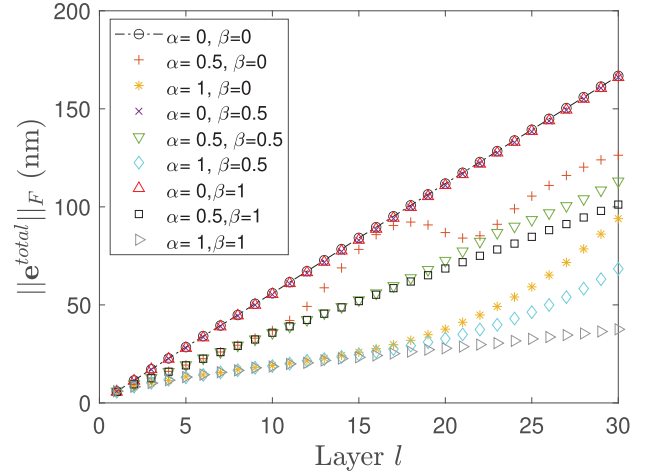

Fig. 7. Total error comparison: HO-SILC results in a lower total error compared with FO-SILC. $\alpha = 0$ and $\beta = 0$ refer to an FO-SILC design that only applies horizontal learning (iteration to iteration; $L = 30$, $q = 1$, $r = 0.01$, and $s = 0.09$).

$\|\mathbf{F}_{0_L}\|_p < 1$ and $\|\Delta H_r\|_p < r_{\text{AIU}_p}$. Note that $(\alpha, \beta) = (0, 0)$ results in an FO-SILC update law that only leverages device-to-device (iteration) learning in the horizontal direction [21]. Unlike [19], we use "dlyap($\mathbf{F}_{0_L}^T, \mathbf{I}$)" in MATLAB to solve the discrete-time Lyapunov equation in (29) and calculate $\mathbf{P}$. In this example, $\mathbf{F}_{0_L}$ is not BCCB, and we cannot use DFT simplifications from [19].

VII. SIMULATION RESULTS

In this section, simulation results of the system described in Sections III and VI-B using HO-SILC are investigated. Tables I–III show that by proper selection of α and β, the

This article has been accepted for inclusion in a future issue of this journal. Content is final as presented, with the exception of pagination.

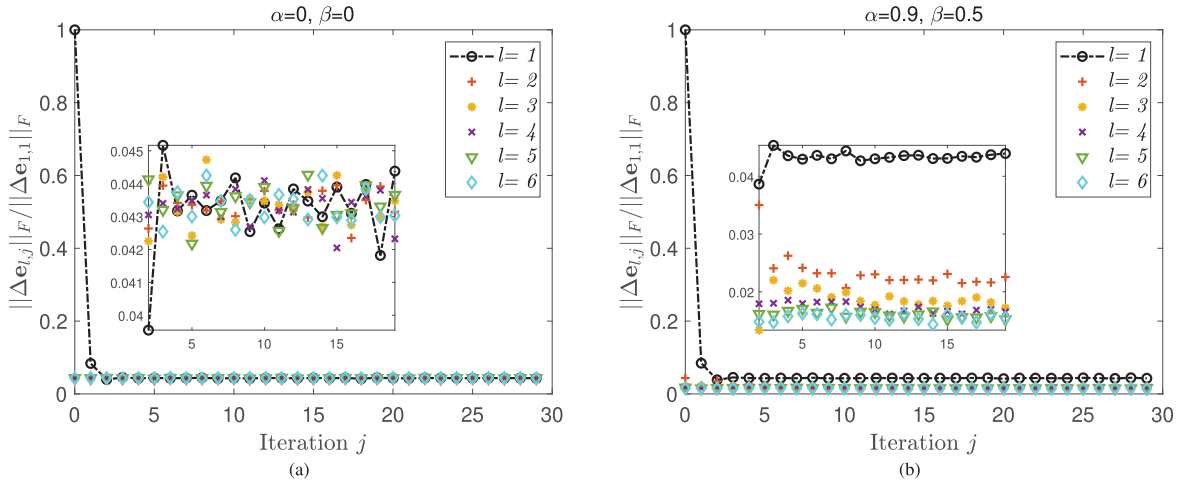AFKHAMI et al.: ROBUST HO-SILC FOR AM SYSTEMS 13

Fig. 8. Convergence of the Frobenius norm of the incremental error: the LPV model in Section VI-A2 is used to design the learning filters in (10). The control update time associated with (10) for updating the feedforward signal per iteration in simulation is 1.34 s. Iteration $j = 0$ refers to the first device ($L = 6$, $q = 1$, $r = 0.01$, and $s = 0.09$). (a) FO-SILC design with $\alpha = 0$ and $\beta = 0$, which only has horizontal learning (iteration to iteration). No learning happens over layers. (b) HO-SILC design with $\alpha = 0.9$ and $\beta = 0.5$. The HO-SILC design integrates horizontal learning from device to device with vertical learning from previous layers. HO-ILC offers better performance over the layers compared with the FO-SILC.

stability radius, r_{AIU}, can be tuned. It is expected that higher values of r_{AIU_p} improve robustness to model uncertainties, while smaller values of $\mathbf{F}_0$, ensuring $\|\mathbf{F}_0\|_p < 1$, increase speed of convergence. In addition, for a constant β, α does not change the maximum singular value of $\mathbf{F}_{0_L}$, $\bar{\sigma} = \|\mathbf{F}_{0_L}\|_2$, which is approximately equal to $\|\mathbf{T}_0^h\|_2$. To be specific, for fixed β, monotonic stability of the nominal system is achieved if $\|\mathbf{T}_0^h\|_2 < 1$. The reason is that the diagonal elements of $\mathbf{F}_{0_L}^T \mathbf{F}_{0_L}$ are equal to $\mathbf{T}_0^{h^2}(\mathbf{I} + \mathbf{T}_0^{v_i^j})$, while off-diagonal elements are the functions of $\mathbf{T}_0^{h^2}(\mathbf{T}_0^{v_i})^j$ for $j = 1, \dots, 2L - 2$. Given $\|\mathbf{T}_0^h\|_2 < 1$ and $\|\mathbf{T}_0^{v_i}\|_2 < 1$, the off-diagonal elements are smaller compared with the main diagonal elements, which results in $\|\mathbf{F}_{0_l}\|_2 \simeq \|\mathbf{T}_0^h\|_2$ based on (37). The simulation results in Tables I–III show that all pairs of (α, β) satisfy $\|\mathbf{F}_0\|_p < 1$. We highlighted the pairs that satisfy the RMC criteria in Theorems 3 and 4, for both l_2 and l_∞ norms. The results show that the l_∞ norm is more conservative than the l_2 norm; therefore, we will focus on the l_2 norm.

In 3-D structures that are fabricated using AM technologies, the error in previous layers adds up in the upper layers and affects the total heightmap and corresponding standard deviations. HO-SILC can improve the total error by incorporating previous layer errors in the cost function in (5). Fig. 7 shows the HO-SILC performance for different values of (α, β). The results show that HO-SILC can improve the overall performance (smaller total heightmap error) when compared with FO-SILC. Based on the provided information in Tables I–III, a lower value of α (while β is fixed) leads to larger r_{AIU}. However, it also degrades the overall performance. Larger values of α impose more weighting on previous layer errors in (4) that results in smaller total errors, $\mathbf{e}_{l,j}$. On the other hand, larger values of β for a constant α result in an increase in the achievable r_{AIU} and decrease the total error. Therefore, by proper tuning of higher-order parameters, the stability robustness and the performance of the HO-SILC with

respect to the total error can be improved. Hereafter, we will set the HO-SILC parameters, $\alpha = 0.9$ and $\beta = 0.5$.

Fig. 8(a) and (b) presents the Frobenius norm of the incremental errors, $\Delta \mathbf{e}_{l,j}$, for FO-SILC and HO-SILC controllers based on the LPV model in Section VI-A2. Fig. 8(a) shows that the final incremental errors of the FO-SILC update law are in the same range over the layers. Fig. 8(b) shows that by using HO-SILC, a significant improvement (around 60% for six layers) in the incremental errors over the layers is achieved. The first layer shows the highest error, with the error signals decreasing due to vertical learning through the iterations. In Fig. 8, the simulation time associated with the controller update in (10) is around 1.34 s, which is 50% faster compared with the control update time (2.85 s) associated with (3) and (9) for the linearized CRRN model in (47). The reason is that the LPV plant model is BCCB, and (10) can be used to update the feedforward signal in Fig. 8.

Fig. 9 shows the performance of the HO-SILC controller designed using a linearized CRNN model (47). Recall that the linearized CRNN model in (47) is from the nonlinear CRNN model used as the *true* model in the simulation. Note that the Jacobian matrix in (47) is not BCCB; thus, DFT calculations are not possible, and the controller derivation requires more time as compared with the HO-SILC algorithm designed with the LPV model in Fig. 8. In addition, the computation time required to calculate the Jacobian matrix in (47) is ≈ 3.5 h, which is a one-time calculation that can be done before running the experiment. The results in Fig. 9 show that, although the HO-SILC based on the linearized CRNN model considers surface tension effects, the controller performance is similar to the HO-SILC based on the LPV model. The reason is that unlike the inkjet printing process used in [25], the e-jet printing process modeled in this work uses high viscosity inks for which the droplets tend to stay at their deposited locations. The reduction in movement on the
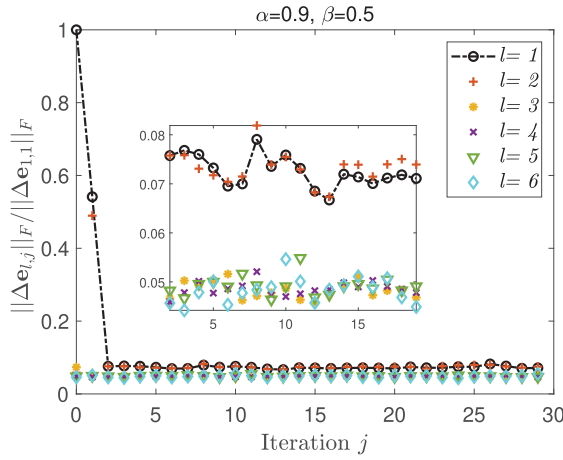
Fig. 9. Performance of the HO-SILC with the linearized CRNN model in (47): convergence of the Frobenius norm of the incremental error with the HO-SILC design in (3) and (8), based on the linearized CRNN model in (47). The average control update time in simulation for updating the feedforward signal per iteration is 2.8 s.

surface post printing reduces the surface tension and droplet coalescence-related effects and shows minimal effects on film formation. Furthermore, model uncertainties due to surface tension of the liquid droplets are often repetitive and, thus, would be learned through the implementation of the HO-SILC. Therefore, it is recommended to use a more simple model, such as LPV in Section VI-A2 or the CLR model in Section VI-A1, to design a robust HO-SILC controller based on the criteria in Theorems 1–4 and Tables I–III that enable the fast DFT calculations in (10).

It should be noted that although the LPV model captures wetting nonlinearities due to existing heightmap nonflatness $[H(\mathbf{g}_{l-1})]$ [29], it is still less accurate compared with the nonlinear CRNN model (see Fig. 6). Here, our aim is to do the following: 1) use a simple BCCB model, such as the LPV (or CLR) model to enable fast DFT computations and still maintain our access to linear control [(46) and (47) are linear with respect to the input signal] and 2) capture the nonlinearities and model mismatches within the interval uncertainty bounds that are described in Theorems 3 and 4. The simulation results show that a control design with either of the LPV or the linearized CRNN model estimations are able to learn the nonlinearities and model mismatches, as demonstrated in Figs. 8 and 9, in which the CRNN is used as the true system, and the other two are used for control design. The controller is able to learn the nonlinearities after a few iterations, and the performance is improved in both cases.

VIII. CONCLUSION

In this article, we present an HO-SILC framework for iteration-varying uncertain AM systems. We consider iteration-varying model uncertainties as interval uncertainties subjected to spatial-invariant bounds. In order to leverage DFT-based tools for computational efficiency, the iteration-varying plant model is considered to be BCCB. An RMC criterion is formalized as a useful tool to predict the stability of the HO-SILC algorithm in the presence of iteration-varying model uncertainties. Our analysis considers the RMC criterion as

a measure of maximum allowable uncertainty around the nominal plant, such that the iterative system remains stable. Simulation results using a model of an e-jet printing system demonstrate that HO-SILC can be successfully employed in AM processes to regulate the input of an iterative model and improve the heightmap reference tracking. We demonstrate that through proper tuning of the higher-order terms of the HO-SILC algorithm, an improved performance in terms of layer to layer and overall height errors can be achieved. The improvements performance is especially prevalent at higher layers, where the uncertainties from previous layer variations are more pronounced. Higher-order, spatial learning control has applications outside of AM systems. For example, any system that exhibits spatially dependent dynamics through a repetitive action (e.g., exoskeletons, robotic pick, and place) could benefit from a control framework that compensates for errors across both a spatial and temporal domain. Importantly, spatial interactions are often disjointed temporally and are commonly ignored. The proposed framework addresses this issue by incorporating spatial information into the control law. Future work will focus on implementation of HO-SILC on an experimental platform.

APPENDIX

Suppose $(f_e, \Delta g_e)$ are the equilibrium pair of (45). For the multilayer structure in Fig. 2, the desired incremental height at all layers and iterations is fixed to Δg^d. Assuming that at the equilibrium, the iteration-varying spatial dynamics converge to a nominal behavior and $\lim_{\substack{l \to \infty \\ j \to \infty}} \Delta g_{l,j} = \Delta g^d$. Since the desired topography is a flat layer with a thickness of $d = 100$ nm $(\Delta g^d = d I_{n \times n})$, there is no height difference across the layer at the equilibrium, and therefore, no droplet-to-droplet movement along the links is expected, $\sigma(l_t) = 0$. In addition, since the reference for all layers is equal, the equilibrium point of layer 1 is equal to the equilibrium point of other layers. Simplifying (45b), at the equilibrium for layer 1, $\mathbf{y}_e^n$ at the equilibrium is calculated as follows:

$$\mathbf{y}_e^n = \ln\left(e^{d+v_0} - \gamma e^{v_0}\right) \mathbf{1}(n, 1) \tag{48}$$

where $\mathbf{y}_e^n$ is the uncured topography at the equilibrium when the last droplet at layer 1 is deposited. Substituting (48) into (45a) and assuming $\sigma(KD^T \mathbf{y}_l^{t-1}) = 0$ at the equilibrium, the input signal at the equilibrium $\mathbf{f}_e$ is calculated as follows:

$$\mathbf{f}_e = W_u^{-1}\ln\left(e^{d+v_0} - \gamma e^{v_0}\right) \mathbf{1}_{n \times 1} \tag{49}$$

where $\mathbf{1}_{n \times 1}$ is a vector of ones.

1) Linearization of the CRNN Model: The linearized approximation model of (45) at $(f_e, \Delta g_e)$, which approximates the dynamics of the nonlinear equation (45) around the equilibrium point, is calculated as follows:

$$\Delta g_l \simeq \left(\frac{\partial g_l}{\partial f_l} - \frac{\partial g_{l-1}}{\partial f_l}\right)_e (f_l - f_e) + \Delta g_e. \tag{50}$$

In addition, $H_J = (\partial g_l)/(\partial f_l)$ is the Jacobian at the equilibrium, and $(\partial g_{l-1})/(\partial f_l) = 0$. The Jacobian matrix is

This article has been accepted for inclusion in a future issue of this journal. Content is final as presented, with the exception of pagination.

AFKHAMI et al.: ROBUST HO-SILC FOR AM SYSTEMS   15

calculated as follows:

$$H_J = \frac{\partial g_l}{\partial f_l} = \frac{\partial g_l}{\partial y_l^n} \frac{\partial y_l^n}{\partial f_l} \tag{51a}$$

$$\frac{\partial g_l}{\partial y_l^n} = \text{diag}\left(\frac{1}{1 + \gamma e^{(v_0 - y_l^n(i))}}\right), \quad i = 1, 2, \ldots, n \tag{51b}$$

$$\frac{\partial y_l^n}{\partial f_l} = W_u - D \sum_{t=1}^{n-1} \sigma'(y_t) K D^T W_u 1_{(1-t)}. \tag{51c}$$

Equation (51b) is consistent with the results in [25]. Equation (51c) is calculated from step-by-step partial derivation of (45b) and (45a). $1_{(1-t)} \in \mathbb{R}^{n \times n}$ in (51) is a block-diagonal matrix with all elements equal to zero, expect the first t diagonal terms, which are equal to one. For example, $1_{(1-1)}$ has only one nonzero element equal to one on $(i, i) = (1, 1)$. Similar to [25], $\sigma'(y_t)$ is as follows:

$$\sigma'(y_t) = \begin{cases} 1, & \text{if } K D^T y_t(i) > \epsilon \\ \delta = 0.01, & \text{if } -\epsilon < K D^T y_t(i) < \epsilon \\ 1, & \text{if } K D^T y_t(i) < -\epsilon. \end{cases} \tag{52}$$

The Jabobian matrix in (51a) is not BCCB, because the second element in (51c) is not BCCB. Note that the linearized equation (50) is an approximation of the nonlinear CRNN model in (45).

ACKNOWLEDGMENT

REFERENCES

[1] I. Gibson, D. Rosen, and B. Stucker, *Additive Manufacturing Technologies: 3D Printing, Rapid Prototyping, and Direct Digital Manufacturing*. 2nd ed. Cham, Switzerland: Springer, 2015.

[2] B. Iezzi, Z. Afkhami, S. Sanvordenker, D. Hoelzle, K. Barton, and M. Shtein, "Electrohydrodynamic jet printing of 1D photonic crystals: Part II—Optical design and reflectance characteristics," *Adv. Mater. Technol.*, vol. 5, no. 10, 2020, Art. no. 2000431.

[3] P. M. Theiler, F. Lütolf, and R. Ferrini, "Non-contact printing of optical waveguides using capillary bridges," *Opt. Exp.*, vol. 26, no. 9, p. 11934, 2018.

[4] K. Wang and J. P. W. Stark, "Direct fabrication of electrically functional microstructures by fully voltage-controlled electrohydrodynamic jet printing of silver nano-ink," *Appl. Phys. A, Solids Surf.*, vol. 99, no. 4, pp. 763–766, Jun. 2010.

[5] J. U. Park, J. H. Lee, U. Paik, Y. Lu, and J. A. Rogers, "Nanoscale patterns of oligonucleotides formed by electrohydrodynamic jet printing with applications in biosensing and nanomaterials assembly," *Nano Lett.*, vol. 8, no. 12, pp. 4210–4216, 2008.

[6] Y. Huang, M. C. Leu, J. Mazumder, and A. Donmez, "Additive manufacturing: Current state, future potential, gaps and needs, and recommendations," *J. Manuf. Sci. Eng.*, vol. 137, no. 1, Feb. 2015, Art. no. 014001.

[7] Y. Wang, F. Gao, and F. J. Doyle, "Survey on iterative learning control, repetitive control, and run-to-run control," *J. Process Control*, vol. 19, no. 10, pp. 1589–1600, Dec. 2009.

[8] M. Norrlöf and S. Gunnarsson, "Time and frequency domain convergence properties in iterative learning control," *Int. J. Control*, vol. 75, no. 14, pp. 1114–1126, Jan. 2002.

[9] D. Meng and K. L. Moore, "Robust iterative learning control for nonrepetitive uncertain systems," *IEEE Trans. Autom. Control*, vol. 62, no. 2, pp. 907–913, Feb. 2017.

[10] H.-S. Ahn, K. L. Moore, and Y. Chen, *Iterative Learning Control: Robustness and Monotonic Convergence for Interval Systems*. Cham, Switzerland: Springer, 2007.

[11] X. Bu, F. Yu, Z. Fu, and F. Wang, "Stability analysis of high-order iterative learning control for a class of nonlinear switched systems," *Abstract Appl. Anal.*, vol. 2013, pp. 1–13, Jan. 2013.

[12] Y.-S. Wei and X.-D. Li, "Robust higher-order ILC for non-linear discrete-time systems with varying trail lengths and random initial state shifts," *IET Control Theory Appl.*, vol. 11, no. 15, pp. 2440–2447, Oct. 2017.

[13] Z. Bien and K. M. Huh, "Higher-order iterative learning control algorithm," *IEE Proc. D-Control Theory Appl.*, vol. 136, no. 3, pp. 105–112, May 1989.

[14] Y. Chen, Z. Gong, and C. Wen, "Analysis of a high-order iterative learning control algorithm for uncertain nonlinear systems with state delays," *Automatica*, vol. 34, no. 3, pp. 345–353, Mar. 1998.

[15] M. Q. Phan and R. W. Longman, "Higher-order iterative learning control by pole placement and noise filtering," *IFAC Proc. Volumes*, vol. 35, no. 1, pp. 25–30, 2002.

[16] K. L. Moore, "An iterative learning control algorithm for systems with measurement noise," in *Proc. 38th IEEE Conf. Decis. Control*, vol. 1, Dec. 1999, pp. 270–275.

[17] M. Norrlof and S. Gunnarsson, "A frequency domain analysis of a second order iterative learning control algorithm," in *Proc. 38th IEEE Conf. Decis. Control*, vol. 2, Dec. 1999, pp. 1587–1592.

[18] D. J. Hoelzle and K. L. Barton, "On spatial iterative learning control via 2-D convolution: Stability analysis and computational efficiency," *IEEE Trans. Control Syst. Technol.*, vol. 24, no. 4, pp. 1504–1512, Jul. 2016.

[19] B. Altin, Z. Wang, D. J. Hoelzle, and K. Barton, "Robust monotonically convergent spatial iterative learning control: Interval systems analysis via discrete Fourier transform," *IEEE Trans. Control Syst. Technol.*, vol. 27, no. 6, pp. 2470–2483, Nov. 2019.

[20] Z. Wang, C. Pannier, L. Ojeda, K. Barton, and D. J. Hoelzle, "An application of spatial iterative learning control to micro-additive manufacturing," in *Proc. Amer. Control Conf. (ACC)*, Jul. 2016, pp. 354–359.

[21] Z. Afkhami, C. Pannier, L. Aarnoudse, D. Hoelzle, and K. Barton, "Spatial iterative learning control for multi-material three-dimensional structures," *ASME Lett. Dyn. Syst. Control*, vol. 1, no. 1, Jan. 2021, Art. no. 011011.

[22] Z. Afkhami, D. Hoelzle, and K. Barton, "Higher-order spatial iterative learning control for additive manufacturing," in *Proc. 60th IEEE Conf. Decis. Control (CDC)*, Dec. 2021, pp. 6547–6553.

[23] E. Rogers and D. H. Owens, *Stability Analysis for Linear Repetitive Processes*, vol. 175. Cham, Switzerland: Springer, 1992.

[24] R. Chi, S. Sui, L. Yu, Z. Hou, and J. Xu, "A discrete-time adaptive ILC for systems with random initial condition and iteration-varying trajectory," *IFAC Proc. Volumes*, vol. 41, no. 2, pp. 14432–14437, 2008.

[25] U. Inyang-Udoh and S. Mishra, "A physics-guided neural network dynamical model for droplet-based additive manufacturing," *IEEE Trans. Control Syst. Technol.*, vol. 30, no. 5, pp. 1863–1875, Sep. 2022.

[26] C. Doumanidis and E. Skordeli, "Distributed-parameter modeling for geometry control of manufacturing processes with material deposition," *J. Dyn. Syst., Meas., Control*, vol. 122, no. 1, pp. 71–77, Mar. 2000.

[27] Y. Guo, J. Peters, T. Oomen, and S. Mishra, "Control-oriented models for ink-jet 3D printing," *Mechatronics*, vol. 56, pp. 211–219, Dec. 2018.

[28] Z. Wang, P. M. Sammons, C. P. Pannier, K. Barton, and D. J. Hoelzle, "System identification of a discrete repetitive process model for electrohydrodynamic jet printing," in *Proc. Annu. Amer. Control Conf. (ACC)*, Jun. 2018, pp. 4464–4471.

[29] C. Pannier, M. Wu, D. Hoelzle, and K. Barton, "LPV models for jet-printed heightmap control," in *Proc. Amer. Control Conf. (ACC)*, Philadelphia, PA, USA, Jul. 2019, pp. 5402–5407.

[30] Z. Afkhami, B. Iezzi, D. Hoelzle, M. Shtein, and K. Barton, "Electrohydrodynamic jet printing of one-dimensional photonic crystals: Part I—An empirical model for multi-material multi-layer fabrication," *Adv. Mater. Technol.*, vol. 5, no. 10, 2020, Art. no. 2000386.

[31] D. A. Bristow, M. Tharayil, and A. G. Alleyne, "A survey of iterative learning control," *IEEE Control Syst. Mag.*, vol. 26, no. 3, pp. 96–114, Jun. 2006.

[32] N. Amann, D. H. Owens, and E. Rogers, "2D systems theory applied to learning control systems," in *Proc. 33rd IEEE Conf. Decis. Control*, vol. 2, Dec. 1994, pp. 985–986.

[33] B. Chu and D. H. Owens, "Iterative learning control for constrained linear systems," *Int. J. Control*, vol. 83, no. 7, pp. 1397–1413, 2010.

[34] A. Cayley, "A memoir on the theory of matrices," *Philos. Trans. Roy. Soc. London*, vol. 9, pp. 100–101, Dec. 1857.

[35] T. Crilly, "Cayley's anticipation of a generalised Cayley-Hamilton theorem," *Historia Math.*, vol. 5, no. 2, pp. 211–219, May 1978.

[36] F. Szabo, *The Linear Algebra Survival Guide: Illustrated With Mathematica*. New York, NY, USA: Academic, 2015.

[37] V. D. Blondel, J. Theys, and J. N. Tsitsiklis, "When is a pair of matrices stable?" in *Unsolved Problems in Mathematical Systems and Control Theory*. Princeton, NJ, USA: Princeton Univ. Press, 2004, p. 304.

[38] D. J. Hoelzle and K. L. Barton, "A new spatial iterative learning control approach for improved micro-additive manufacturing," in *Proc. Amer. Control Conf.*, Jun. 2014, pp. 1805–1810.

David J. Hoelzle (Member, IEEE) received the B.S. degree in mechanical engineering from The Ohio State University, Columbus, OH, USA, in 2005, and the M.S. and Ph.D. degrees in mechanical science and engineering from the University of Illinois at Urbana-Champaign, Champaign, IL, USA, in 2007 and 2011, respectively.
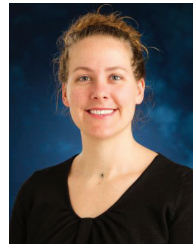
Between his Ph.D. and current position, he was a Post-Doctoral Researcher with the Department of Integrative Biology and Physiology, University of California at Los Angeles, Los Angeles, CA, USA, and an Assistant Professor with the Department of Aerospace and Mechanical Engineering, University of Notre Dame, Notre Dame, IN, USA. He is currently an Associate Professor with the Department of Mechanical and Aerospace Engineering, The Ohio State University. His research interests include applied control theory and dynamics for applications in additive manufacturing robotics and microsystems for mechanobiology research.

Prof. Hoelzle was a recipient of the 2016 CAREER Award, the 2016 Society of Manufacturing Engineers (SME) Outstanding Young Manufacturing Engineer Award, and the 2019 Lumley Research Award.

Kira Barton (Senior Member, IEEE) received the B.Sc. degree in mechanical engineering from the University of Colorado Boulder, Boulder, CO, USA, in 2001, and the M.Sc. and Ph.D. degrees in mechanical engineering from the University of Illinois at Urbana-Champaign, Urbana, IL, USA, in 2006 and 2010, respectively.

From 2010 to 2011, she was a Post-Doctoral Researcher with the University of Illinois at Urbana-Champaign. She is currently an Associate Professor with the Department of Mechanical Engineering, University of Michigan, Ann Arbor, MI, USA. Her research interests include modeling, sensing, and control for applications in advanced manufacturing and robotics, with a specialization in iterative learning control and microadditive manufacturing.

Dr. Barton was a recipient of the National Science Foundation (NSF) CAREER Award in 2014, the 2015 Society of Manufacturing Engineers (SME) Outstanding Young Manufacturing Engineer Award, the 2015 University of Illinois Department of Mechanical Science and Engineering Outstanding Young Alumni Award, the 2016 University of Michigan Department of Mechanical Engineering Department Achievement Award, and the 2017 the American Society of Mechanical Engineers (ASME) Dynamic Systems and Control Young Investigator Award.

Zahra Afkhami (Member, IEEE) received the B.S. degree in mechanical engineering from the Golpayegan University of Technology, Isfahan, Iran, in 2011, the M.S. degree in mechanical engineering from Shiraz University, Shiraz, Iran, in 2013, and the M.S. degree in mechanical engineering from the University of Michigan, Ann Arbor, MI, USA, in 2018, where she is currently pursuing the Ph.D. degree in mechanical engineering under the supervision of Prof. Barton.

Her research interests include modeling and control with application to microadditive manufacturing processes with specialization in iterative learning control and model predictive control.